Image-Derived Forces in an Elastic Image Registration Model

Vegard Vaaland Öztan

Master Thesis in Applied and Computational Mathematics,
Department of Mathematics,
University of Bergen,
June 2021

Abstract

In this work, we explore the role of image-derived forces in an elastic image registration model, and investigate the possibility of accurately estimating displacement fields. Further, we propose a novel, physically motivated, image registration method where the resulting displacement is controlled by the boundary conditions. This is in contrast to traditional methods, where the displacement is driven by an unphysical image-derived body force. Several registration experiments are done, both to highlight the role of image-derived forces, and to demonstrate the capabilities of the novel method. Additionally, the method is used to explore the effects of optimizing over tissue parameters.

Experiments show us that there is a poor agreement between similarity error and displacement field error when performing traditional elastic registration. The novel method produces satisfactory visual registration results, comparable to existing methods. The method ensures that the resulting displacement field is physically possible and obeys the governing equations, however, this is at the cost of a worse performance in terms of minimization of the chosen distance measure.

Acknowledgments

I would like express my gratitude to my two supervisors, Erik A. Hanson and Erlend Hodneland, for their continuous guidance and support during the past year. Thank you, Erik, for introducing me to the field of image registration, and always discussing new and interesting ideas with me. Thank you, Erlend, for always being available to help me with my problems, your genuine interest has been a big motivating factor. The help from you both have been invaluable.

I would also like to thank my fellow students for making the past five years so enjoyable. Lastly, a big thank you to my family for always supporting me.

Vegard Vaaland Öztan
Bergen, June 2021

Contents

List of Figures

List of Symbols

$\mathcal{R}$	Reference image
$\mathcal{T}$	Moving image
$\mathcal{T}_{\boldsymbol{u}}$	Transformed image
$\mathcal{D}$	Distance measure
$\mathcal{S}$	Regularizer
α	Regularization parameter
$\boldsymbol{\sigma}$	Stress tensor
$\boldsymbol{\varepsilon}$	Strain tensor
$\boldsymbol{T}$	Traction vector
$\boldsymbol{u}$	Displacement field
λ	First Lamé parameter
μ	Second Lamé parameter
E_{disp}	Relative displacement field error
E_{img}	Relative image intensity error

Introduction

Image registration is the process of aligning images taken from the same scene. The images could differ as a result of them being taken at different times, from different viewpoint, and/or from different sensors [1]. Alignment of the images is necessary in order to extract spatially dependent information about the image subject. Combining images taken form different sensors will give us a richer source of information [2].

There are a large number of applications where registration is needed. Some examples include biology, criminology, astronomy, art, medicine, and other areas that invokes imaging techniques [3]. Although this thesis has a focus on medical image registration, the ideas and methods presented can easily be transferred to other areas.

Minimally invasive procedures are becoming increasingly important in modern healthcare [4]. It opens up for the possibility of giving patients more precise diagnoses and treatments at an earlier stage, while minimizing the need for surgical procedures. Medical image registration can become an invaluable tool in this context, by extending the concept of image registration to not only be a method for image alignment, but also to become the task of estimating the deformation that has occurred [5]. However, this is not a trivial task, and studies have found that existing algorithms will align images with high precision, and at the same time obtain a displacement field with a relative error of 40 % [5].

Human organs and tissue obey the laws of physics when they are deformed, and it would be natural to model this deformation with image registration tools. Popular existing methods based on minimization of energy functionals, like elastic registration [6], are physically motivated, and borrows ideas from continuum mechanics, but at the same time introduces unphysical image-derived forces to drive the registration forward. In other words, existing registration methods mixes physical quantities with unphysical forces, and in thesis will explore how these forces affects the registration results, and how to avoid them.

Starting from the fundamental concepts of elasticity and energy minimization,

we derive the elastic registration method, and discuss the image-derived forces that arise. Experiments are done with the elastic method to explore the role of these forces, and test the capability of accurately estimating displacement fields. Further, a novel registration method is presented and demonstrated. It is based on actively using the boundary conditions and solving the governing equations to drive the registration forward, as opposed to the unphysical body force used in traditional methods.

Thesis outline

Chapter 1: contains the background theory and fundamental concepts used throughout this thesis. Specifically, section 1.1 presents a mathematical framework for image registration, section 1.2 introduces the basics of elasticity and presents the governing equations. In section 1.3, a brief introduction to calculus of variations and the concepts of energy minimization are given. Finally, section 1.4 covers the numerical methods used in this thesis.

Chapter 2: covers elastic image registration. Using the fundamentals from elasticity and energy minimization, the traditional elastic image registration method is derived, and the arising image-derived forces are discussed along with some disadvantages of the method. Our novel contribution is then presented, a boundary-driven image registration (BDIR) method.

Chapter 3: contains several image registration experiments. In section 3.1, the role of image-derived forces when performing elastic registration is explored by investigating the agreement between image similarity and displacement field error. In section 3.2, the BDIR method is demonstrated and compared to the traditional method. This is done on both synthetic and real data. In section 3.3, BDIR is used to explore the effects of optimizing over tissue parameters. Finally, the results are discussed in section 3.4.

Chapter 4: summarizes the work done in this thesis, discusses some of its limitations and we propose further ideas to be investigated.

Chapter 1

Background Theory

In this chapter, we present the background theory and fundamental concepts that are needed to derive and solve the problems this thesis is concerned with. It is divided as follows:

Section 1.1 provides a mathematical framework for image registration, where the registration problem is formally stated. Different distance measures are discussed along with the inherent ill-posedness of the problem. Regularization techniques are presented, and finally a discussion around evaluation metrics is had.

In section 1.2, the theory of elasticity is presented. Starting form the concepts of stress and traction, we introduce concepts such deformation, strain, and Hooke's law. Finally, the governing equations of linear elasticity are derived.

Section 1.3 gives a brief overview of calculus of variations and energy minimization principles, which we use to derive the Navier-Lamé equations.

Finally, in section 1.4, the numerical methods used in this thesis are presented. It is divided into two section, quasi-Newton methods for solving minimization problems, and multi-point stress approximation for solving the elasticity equations.

1.1 Mathematical framework for image registration

In this section, a general mathematical framework for image registration is presented. Starting with the definition of an image, the general registration problem is formally stated. Different distance measures are covered, and the inherent ill-posedness of the problem is discussed. The elastic regularizer is presented, along with other regularization choices. Finally, some evaluation metrics are discussed.

Only the general idea of elastic registration is covered in this chapter, and in chapter 2 we go into greater detail about elastic registration as we then are equipped with the necessary concepts to derive the method.

1.1.1 Problem statement

Definition 1 (Image)**.** *An image is a continuous function* $\mathcal{I} : \Omega \to \mathbb{R}$*, where* $\Omega \subset \mathbb{R}^d$ *and* $d \in \mathbb{N}$*.*

The definition above can be extended to a time-dependent image as follows

Definition 2 (Time-dependent image)**.** *A time-dependent image is a continuous function* $\mathcal{I} : \Omega \times T \to \mathbb{R}$*, where* $\Omega \subset \mathbb{R}^d$*,* $T \in \mathbb{R}_{\geq 0}$*, and* $d \in \mathbb{N}$*.*

We denote Ω as the image domain and d the spacial dimensions of the image, typically $d = 2$ or $d = 3$. For an image $\mathcal{I}$, we have at each spacial position $\boldsymbol{x} = (x_1, x_2, \ldots, x_d) \in \Omega$ an associated intensity value $\mathcal{I}(\boldsymbol{x}, t)$ for some time t. For simplicity, the following derivations are presented with time-independent images.

The general problem in image registration can be formulated as follows: Given a reference image $\mathcal{R}$ and moving image $\mathcal{T}$, we search for a transformation φ, defined as

$$\varphi : \Omega \to \mathbb{R}^d, \qquad \varphi(\boldsymbol{x}) = \boldsymbol{x} + \boldsymbol{u}(\boldsymbol{x}), \tag{1.1}$$

that depends on the unknown displacement field

$$\boldsymbol{u} : \Omega \to \mathbb{R}^d, \tag{1.2}$$

such that the transformed moving image

$$\mathcal{T} \circ \varphi(\boldsymbol{u}(\boldsymbol{x})) = \mathcal{T}(\boldsymbol{x} + \boldsymbol{u}(\boldsymbol{x})) = \mathcal{T}_{\boldsymbol{u}}, \tag{1.3}$$

becomes similar to $\mathcal{R}$. Note that with this Eulerian framework, $\boldsymbol{u}$ is used to model the transformation φ as it describes how a point in the transformed moving $\mathcal{T}_{\boldsymbol{u}}$ is moved away from its original position. Thus, finding the displacement field $\boldsymbol{u}$ and the transformation φ is equivalent.

1.1.2 Distance measures

All registration techniques requires a suitable distance measure $\mathcal{D}$, sometimes called similarity measure, which measures the similarity of $\mathcal{T}_{\boldsymbol{u}}$ and $\mathcal{R}$ over the image domain Ω. At its simplest form, the image registration problem can be formulated as follows

$$\min_{\boldsymbol{u}} \mathcal{D}(\mathcal{T}_{\boldsymbol{u}}, \mathcal{R}). \tag{1.4}$$

How to measure the similarity of images is not a trivial task, and there is no unified approach that will work for all types of images. In general we can differentiate between two types of images. Monomodal images have similar intensities and contrast, and is typically captured with the same device. Multimodal images on the other hand does not have comparable intensities and contrast. This can be a result of the images not being taken by the same device, or from a device with different exposure settings. The distance measure must be chosen on a case by case basis depending on the images to be registered.

Sum of Squared Distances

The sum of squared distances (SSD) compares intensity values of two images, and is given by

$$\mathcal{D}^{SSD}(\mathcal{T}, \mathcal{R}) = \frac{1}{2} \int_{\Omega} (\mathcal{T}(\boldsymbol{x}) - \mathcal{R}(\boldsymbol{x}))^2 \, d\boldsymbol{x} = \frac{1}{2} \big\| \mathcal{T}(\boldsymbol{x}) - \mathcal{R}(\boldsymbol{x}) \big\|_2^2 . \tag{1.5}$$

For this distance measure to give a meaningful result, the intensity values of the images has to be comparable. This is not always the case, especially when dealing with multimodal images.

In this thesis we are exclusively dealing with monomodal images, and the SSD will be distance measure used unless stated otherwise.

Mutual Information

The Mutual Information (MI) distance measure work by the comparing statistical dependence of two images. It makes no assumptions about the imaging process, making it a popular choice for multimodal images. See books by Modersitzki for more details [3, 6].

Normalized Gradient Fields

The normalized gradient fields (NGF) distance measure, proposed by Haber and Modersitzki [7], is based on the assumption that images of different modalities still has intensity changes in corresponding positions, and the intensity changes

are given by the image gradient $\nabla\mathcal{T}$. This makes the NGF measure especially suitable for multimodal images. A normalization of the gradient is done as we are only interested in the direction, not the strength, and is given by

$$\bar{\nabla}\mathcal{T} = \frac{\nabla\mathcal{T}(\boldsymbol{x})}{\sqrt{\left\|\mathcal{T}(\boldsymbol{x})\right\|^2 + \eta^2}}, \tag{1.6}$$

where η is an edge parameter controlling the influence of image gradients [8]. The NGF distance measure is given by

$$\mathcal{D}^{NGF}(\mathcal{T},\mathcal{R}) = \int_\Omega 1 - \left(\bar{\nabla}\mathcal{T}(\boldsymbol{x})^T \cdot \bar{\nabla}\mathcal{R}(\boldsymbol{x})\right)^2 d\boldsymbol{x}. \tag{1.7}$$

1.1.3 Ill-posedness

When working on a mathematical problem it is desired, often necessary, that the problem is well-posed. Following Hadamards definition, a problem is well posed if it possesses all of the following properties [9]

1. a solution exists,
2. the solution is unique,
3. the solutions varies continuously with the initial data.

Problems that are not well posed are called ill-posed.

It is well known that the minimization problem in (1.4) is ill-posed in the sense that direct minimization of $\mathcal{D}$ will not result in a unique solution for $\boldsymbol{u}$. A simple example illustrating this fact is shown in Figure 1.1. Here we see two square boxes which we want to register. A simple translation to the left of the moving image will result in a perfect registration. However, the same translation with an added rotation of 180° will also result in a perfect registration, and hence the problem is clearly ill-posed.

Another important point to make about the ill-posedness of image registration is the fact that in areas of constant intensity, any displacement will not change the result. Meaning that in the area where both $\mathcal{R}$ and $\mathcal{T}$ in Figure 1.1 is completely black, the displacement field could be arbitrary, and it would not impact the solution.

1.1.4 Regularization

To overcome the ill-posed nature of image registration, it is necessary to impose regularization of $\boldsymbol{u}$ to penalize unwanted and irregular solutions. Regularization

Figure 1.1: Two squares to be registered. Several displacement fields will result in a perfect registration, and hence the problem is clearly ill-posed.

can be seen as adding information to the problem, or restricting the function space we are searching over. In image registration, this is done by adding a regularization functional $\mathcal{S}(\boldsymbol{u})$ to (1.4), giving us the minimization problem of the joint functional

$$\min_{\boldsymbol{u}} \left\{ \mathcal{J}(\boldsymbol{u}) = \mathcal{D}(\mathcal{T}_{\boldsymbol{u}}, \mathcal{R}) + \alpha \mathcal{S}(\boldsymbol{u}) \right\}, \tag{1.8}$$

where α is a regularization parameter that balances similarity and regularity.

As an example, let us imagine that the white box in Figure 1.1 is physically incapable of rotating. In this case we would want to use a regularizer that penalizes all rotations. The solution to the problem will now, hopefully, be the one that only translates the box. Other examples includes cases where we want the resulting displacement field to be sufficiently smooth. It is clear that $\mathcal{S}$ needs to be chosen based on a priori knowledge of the image subject.

Elastic regularizer

The elastic regularizer, which was first used in image registration by Broit [10], measures the elastic potential energy introduced by deforming an elastic material, and is given by

$$\mathcal{S}^{elas}(\boldsymbol{u}) = \int_{\Omega} \frac{\mu}{4} \left(u_{i,j} + u_{j,i}\right) \left(u_{i,j} + u_{j,i}\right) + \frac{\lambda}{2} u_{i,i} u_{k,k} \, d\boldsymbol{x}, \tag{1.9}$$

where λ and μ are the first and second Lamé parameter respectively. Note that Einstein notation is used here, where a repeated index implies summation. This regularizer is a key part of this thesis, and a more detailed discussion will be had in chapter 2, where the physical motivation behind it will be covered, and the elastic registration method is derived.

Fluid regularizer

The linear elastic regularizer does not allow for larger deformations which may render it unusable in cases where the deformations are too large. To overcome this fact, Christensen [11] proposed a regularizer using a viscous fluid model based on a specific linearization of the Navier-Stokes equation [12]. The fluid regularizer is obtained by taking the elastic potential of the velocity field $\boldsymbol{v}$ of the displacement field $\boldsymbol{u}$

$$\mathcal{S}^{fluid}(\boldsymbol{u}) = \mathcal{S}^{elas}(\boldsymbol{v}), \tag{1.10}$$

where the velocity is related to the now time dependent displacement filed through the material derivative

$$\frac{D\boldsymbol{u}(\boldsymbol{x},t)}{Dt} = \frac{\partial \boldsymbol{u}(\boldsymbol{x},t)}{\partial t} + \nabla \boldsymbol{u}(\boldsymbol{x},t)\boldsymbol{v}(\boldsymbol{x},t). \tag{1.11}$$

Diffusion regularizer

In contrast to the elastic and fluid regularizers which is physically motivated, the diffusion regularizer is motivated by the smoothness of the displacement field itself [6]. Diffusion registration was first introduced by Fischer and Modersitzki [13] and its regularizer is given by

$$\mathcal{S}^{diff}(\boldsymbol{u}) = \frac{1}{2}\int_{\Omega} \|\nabla \boldsymbol{u}\|_2^2 \, d\boldsymbol{x}. \tag{1.12}$$

Curvature regularizer

Curvature registration, first introduced by Fisher and Modersitzki [14], produces even smoother displacement fields than diffusion registration, and its regularizer is given by

$$\mathcal{S}^{curv}(\boldsymbol{u}) = \frac{1}{2}\int_{\Omega} \left\|\nabla^2 \boldsymbol{u}\right\|_2^2 \, d\boldsymbol{x}, \tag{1.13}$$

where $\nabla^2 = \nabla \cdot \nabla$ is the Laplace operator. The curvature regularizer has the interesting property of not penalizing affine linear transformations, unlike the other introduced regularizers [14]. This means that affine linear pre-registration is not needed when using the curvature regularizer.

1.1.5 Evaluation metrics

Evaluation of image registration results is a challenging task due to the lack of ground truth displacement fields. Only using the distance measure as an evaluation tool will cause problems because of the ill-posed nature of image registration. There exists several methods for measuring registration results, however, they have

been shown to be unreliable. In experiments done by T. Rohlfing, it is shown that a registration algorithm that purposely generates highly inaccurate displacement fields, still performs well in terms of the existing measures [15]. The registration algorithm was appropriately named CURT, or Completely Useless Registration Tool. In this thesis, we only define an evaluation metric for displacement fields in cases where the true displacement is known, i.e. in synthetic cases.

Let $\mathcal{I}^*$ and $\boldsymbol{u}^*$ denote a reference image and displacement field respectively. We measure the relative displacement field error as

$$E_{disp}(\boldsymbol{u}, \boldsymbol{u}^*) = \frac{\|\boldsymbol{u} - \boldsymbol{u}^*\|_2}{\|\boldsymbol{u}^*\|_2}, \tag{1.14}$$

where $\boldsymbol{u}$ is some displacement field to be compared against the reference. The relative image intensity error is defined as

$$E_{img}(\mathcal{I}, \mathcal{I}^*) = \frac{\|\mathcal{I} - \mathcal{I}^*\|_2}{\|\mathcal{I}^*\|_2}, \tag{1.15}$$

where $\mathcal{I}$ is some image to be compared against the reference.

1.2 Elasticity

A body is said to be perfectly elastic if it returns to its initial original shape after the external sources of deformation disappears [16]. In this section we present the fundamental concepts that describe such a body. We start by introducing fundamental concepts such as stress, strain, deformation, and Hooke's law, before we present the governing equations for an isotropic linearly elastic body. The theory from this section is mainly based on [17, 18].

1.2.1 Stress

A body subject to some force can be seen as transmitting these forces from one point to another. Stress is intended to quantify the interaction between the points that make up the body when it is subject to external loading [17].

We differentiate between two types of stress, normal and shear stress. To illustrate the difference, let us consider a planar cross-section of area A and a small region of area ΔA centered at point c somewhere on the cross-section. Further, let F_n be the normal force acting on the cross-section. The normal stress σ_n at point c is defined as

$$\sigma_n = \lim_{\Delta A \to 0} \frac{\Delta F_n}{\Delta A}, \tag{1.16}$$

where ΔF_n is the total normal force acting on the smaller region. Shear stress σ_s is defined in a similar manner, however let us now consider a shear force F_s acting on the cross-section. The shear force at point c is defined as

$$\sigma_s = \lim_{\Delta A \to 0} \frac{\Delta F_s}{\Delta A}, \tag{1.17}$$

where ΔF_s is defined as the shear force acting on the smaller region.

Stress tensor

Consider a three-dimensional infinitesimal cubic volume element. Figure 1.2 shows all stresses acting on the faces of the cube. Here we recognize both normal and sheer stress. The first subscript indicates the direction of the stress and the second subscript refers to the direction normal to the cross-section.

Note that the faces not shown in the figure also have corresponding stresses. If the cube is stationary, and no internal forces are acting on it, the stresses on the

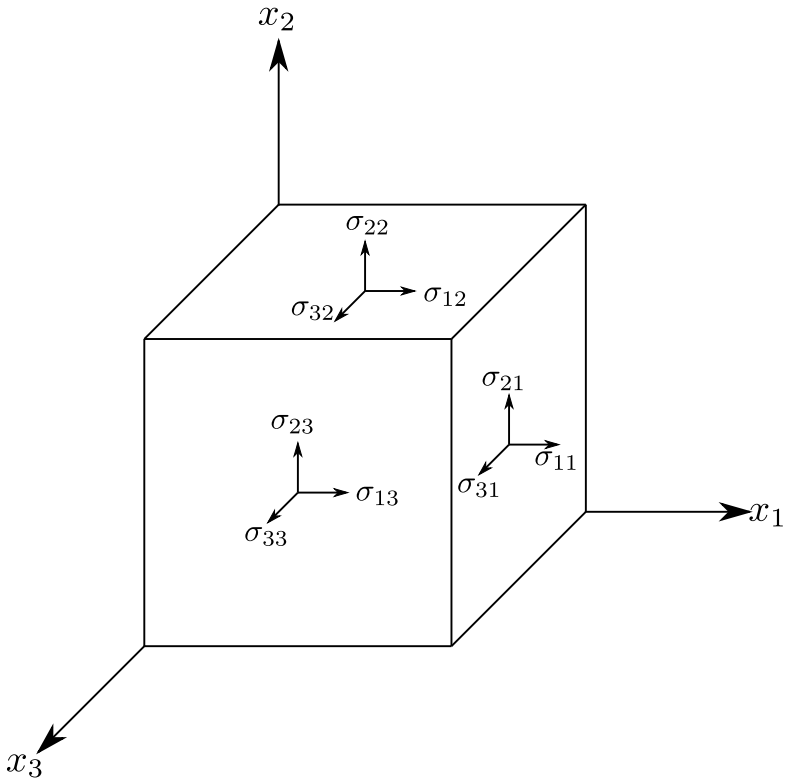

Figure 1.2: Components of the stress tensor acting on a three-dimensional volume element. Adapted from *Continuum Mechanics and thermodynamics* [19].

hidden faces are equal in magnitude but opposite in direction to the ones shown. In matrix form, we can express all components of the stress with the stress tensor

$$\boldsymbol{\sigma} = \begin{bmatrix} \sigma_{11} & \sigma_{12} & \sigma_{13} \\ \sigma_{21} & \sigma_{22} & \sigma_{23} \\ \sigma_{31} & \sigma_{32} & \sigma_{33} \end{bmatrix}, \tag{1.18}$$

which is often called the Cauchy stress tensor.

1.2.2 Traction vector

To introduce the traction vector, sometimes called the stress vector, let us consider a infinitesimal subbody in the shape of a right triangle, where the legs are parallel to the x_1 and x_2-axis, see Figure 1.3. Assume the area of the inclined plane is dA, with unit normal vector $\boldsymbol{n}$. The resultant force acting on the plane is denoted $\boldsymbol{T}dA$, where $\boldsymbol{T}$ is called the traction vector.

If we assume the body is in force equilibrium, the forces must sum to zero

$$T_1 dA = \sigma_{11} dA \cos\theta + \sigma_{12} dA \sin\theta, \tag{1.19}$$
$$T_2 dA = \sigma_{21} dA \cos\theta + \sigma_{22} dA \sin\theta. \tag{1.20}$$

Dividing by dA and using the fact that $n_1 = \cos\theta$ and $n_2 = \sin\theta$, we get

$$T_1 = \sigma_{11} n_1 + \sigma_{12} n_2, \tag{1.21}$$
$$T_2 = \sigma_{21} n_1 + \sigma_{22} n_2, \tag{1.22}$$

or in matrix form as

$$\begin{bmatrix} T_1 \\ T_2 \end{bmatrix} = \begin{bmatrix} \sigma_{11} & \sigma_{12} \\ \sigma_{21} & \sigma_{22} \end{bmatrix} \begin{bmatrix} n_1 \\ n_2 \end{bmatrix}. \tag{1.23}$$

This can easily be extended to a three-dimensional case by using a tetrahedron instead of a right triangle. In that case, the traction vector becomes

$$\begin{bmatrix} T_1 \\ T_2 \\ T_3 \end{bmatrix} = \begin{bmatrix} \sigma_{11} & \sigma_{12} & \sigma_{13} \\ \sigma_{21} & \sigma_{22} & \sigma_{23} \\ \sigma_{31} & \sigma_{32} & \sigma_{33} \end{bmatrix} \begin{bmatrix} n_1 \\ n_2 \\ n_3 \end{bmatrix}, \tag{1.24}$$

or equivalently in vector notation

$$\boldsymbol{T} = \boldsymbol{\sigma} \cdot \boldsymbol{n}, \tag{1.25}$$

which knows as the Cauchy stress formula [20].

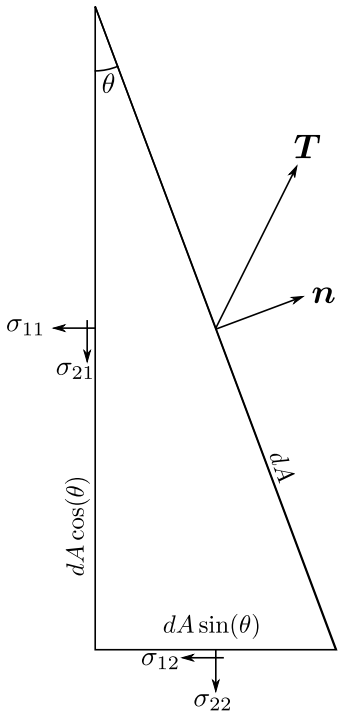

Figure 1.3: Traction vector acting on triangular segment. Adapted from *Introduction to Solid Mechanics* [17].

1.2.3 Deformation and Strain

Deformation can be defined as a change in the distances between material points which lead to changes in shape and/or size of a body. All materials are deformed to some extent when subjected to a force, and be introducing the concept of strain, we can quantify the deformation of a solid relative to some reference frame. [17].

Let us consider an isotropic bar, meaning the material properties are independent of direction [20], of length L with tensile forces acting on it at both ends, stretching it by an amount ΔL as shown in Figure 1.4.

The relative stretch λ is defined as

$$\lambda = \frac{L + \Delta L}{L} = 1 + \frac{\Delta L}{L}, \tag{1.26}$$

where elongation per unit length, $\varepsilon_{long} = \frac{\Delta L}{L}$, is independent of the length of the bar [17]. This quantity is known as longitudinal strain.

To consider more arbitrary deformations we look at the positions of some points in a body before and after it has been deformed in some way. Let a point be denoted

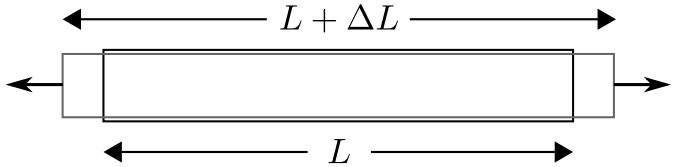

Figure 1.4: Stretching of a bar with an applied force at both ends. Adapted from [17].

a in the undeformed body, which is moved to a new position a' in the deformed body. Let the displacement $\boldsymbol{u}$ of a point be given as

$$\boldsymbol{u}(a) = a' - a, \tag{1.27}$$

which describes the motion of the point after the body changes its shape. As with the stretched bar, we are interested in the relative displacement of the points, which is captured by the strain [18]. To derive the expression, consider now two points a and b, and the line element between them $\boldsymbol{l} = b - a$. After the deformation of the body, the points have moved relative to each other and we now have points a' and b' separated by the line $\boldsymbol{l}' = b' - a'$ as shown in Figure 1.5.

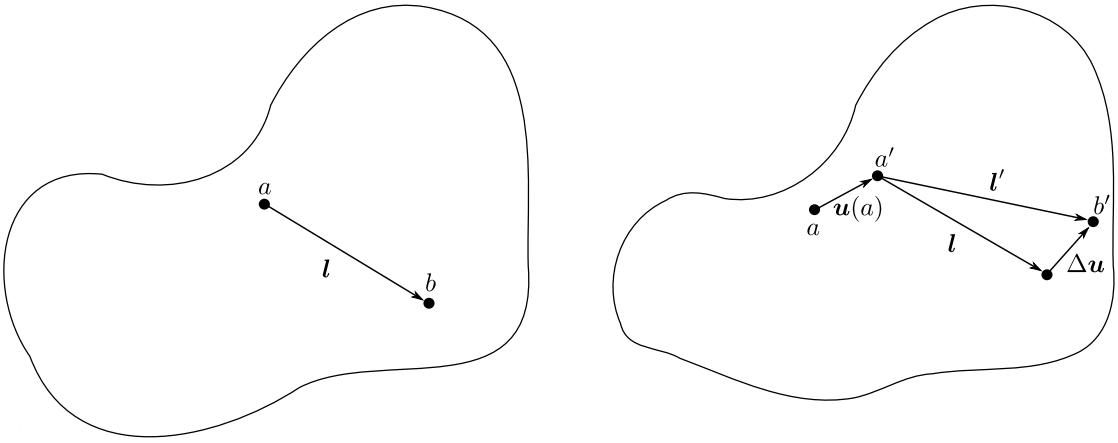

Figure 1.5: An elastic body undergoing some deformation. Left is before deformation and right is after. Adapted from *Desiccation Cracks and Their Patterns* [18].

The relative displacement, or change of the line element, is now given by

$$\Delta\boldsymbol{u}(a, b) = \boldsymbol{u}(b) - \boldsymbol{u}(a) = \boldsymbol{l}' - \boldsymbol{l} \tag{1.28}$$

Further, looking at the length of $\boldsymbol{l}$ and $\boldsymbol{l}'$

$$L = \|\boldsymbol{l}\| = \sqrt{l_i l_i}$$
$$L' = \left\|\boldsymbol{l}'\right\| = \sqrt{l'_i l'_i} = \sqrt{(l + \Delta u)_i (l + \Delta u)_i} = \sqrt{L^2 + 2 l_i \Delta u_i + \Delta u_i \Delta u_i}$$

Next we assume the deformations are infinitesimally small, meaning $\|\Delta \boldsymbol{u}\| \ll L$, which allows us to Taylor expand L' around the equilibrium length L

$$L' = L + \frac{1}{2L}(2l_i \Delta u_i) + \mathcal{O}(\|\Delta \boldsymbol{u}\|^2), \tag{1.29}$$

and neglect higher order terms. A rearrangement gives us an expression for the relative difference in lengths

$$\frac{L' - L}{L} = \frac{1}{L^2}(l_i \Delta u_i), \tag{1.30}$$

and we can Taylor expand Δu_i

$$\Delta u_i = \frac{\partial u_i}{\partial x_j} l_j + \mathcal{O}(\|\Delta \boldsymbol{u}\|^2). \tag{1.31}$$

Equation (1.31) can be inserted in (1.30), and by the symmetry of $(\partial u_i/\partial x_j) l_i l_j = (\partial u_j/\partial x_i) l_j l_i$, we have the explicit form of the linear strain tensor

$$\varepsilon_{ij} = \frac{1}{2}\left(\frac{\partial u_i}{\partial x_j} + \frac{\partial u_j}{\partial x_i}\right), \tag{1.32}$$

or in vector form

$$\boldsymbol{\varepsilon} = \frac{1}{2}\left(\nabla \boldsymbol{u} + (\nabla \boldsymbol{u})^T\right), \tag{1.33}$$

which is valid for small deformations, i.e. $|\nabla \boldsymbol{u}| \ll 1$. Rigid body translations and rotations will not introduce any strains, which is to be expected as such displacements does not change the distance between points in a body.

1.2.4 Hooke's Law

Hooke's law states that for relativity small deformations of an elastic body, the strain is proportional to the stress applied to it [19]. An alternative formulation is that the displacement is proportional to the deforming force. Hooke's law is derived by first considering the uniaxial and shear case, before deriving the generalized Hooke's law.

Uniaxial and shear Hooke's law

Let us consider a rectangular linearly elastic bar. The left side of the bar is clamped, while at the right side a constant force F is applied. This results in the bar being stretched a distance ΔL, as illustrated in Figure 1.6. Hooke's law states that the longitudinal strain $\varepsilon_{long} = \Delta L/L$ is proportional to the stress F/A

applied to it. The constant of proportionality E is called Young's modulus. This gives us the uniaxial Hooke's law

$$\sigma_{ii} = E\varepsilon_{ii} \tag{1.34}$$

There is also a shear version of Hooke's law which reads

$$\sigma_{ij} = 2G\varepsilon_{ij}, \tag{1.35}$$

where G is the shear modulus, which is identical to the second Lamé parameter μ.

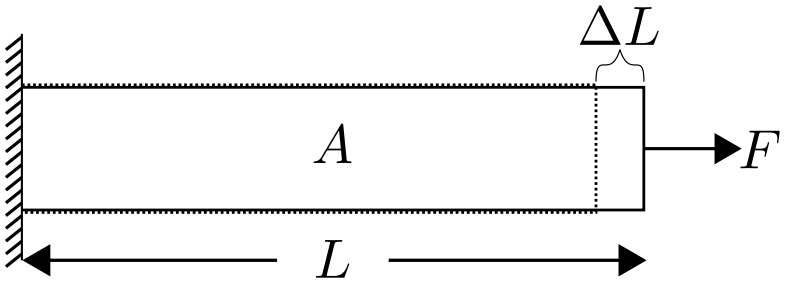

Figure 1.6: Loaded bar being stretched. Adapted from *Introduction to solid mechanics* [17].

Generalized Hooke's law

In general, all the components of the strain tensor can be non-zero, and hence we a relation for this case. To do so, we first need to introduce Poisson's ratio.

When compressing an elastic body, it tends expand in the direction perpendicular to the force applied, and vice versa. This is called the Poisson effect. Poisson's ratio describes the amount of transverse contraction/elongation when strained in a given direction [17]. Mathematically it is given as

$$\nu = -\frac{\varepsilon_{trans}}{\varepsilon_{long}}, \tag{1.36}$$

where ε_{trans} transverse strain, and ε_{long} is longitudinal strain.

Let us now consider the isotropic volume element in Figure 1.2. Taking the Poisson effect into account, we see that by combing (1.34) and (1.36), the stress σ_{11} produce the strains

$$\varepsilon_{11} = \frac{\sigma_{11}}{E} \quad \varepsilon_{22} = -\nu\frac{\sigma_{11}}{E} \quad \varepsilon_{33} = -\nu\frac{\sigma_{11}}{E}. \tag{1.37}$$

Equivalently, the stresses σ_{22} and σ_{33} will produce the strains

$$\varepsilon_{11} = -\nu\frac{\sigma_{22}}{E} \quad \varepsilon_{22} = \frac{\sigma_{22}}{E} \quad \varepsilon_{33} = -\nu\frac{\sigma_{22}}{E} \tag{1.38}$$

and

$$\varepsilon_{11} = -\nu\frac{\sigma_{33}}{E} \quad \varepsilon_{22} = -\nu\frac{\sigma_{33}}{E} \quad \varepsilon_{33} = \frac{\sigma_{33}}{E}, \tag{1.39}$$

respectively. The principle of superposition allows us to add the strains produced by the stresses acting on each direction independently. Using this principle on equations (1.37) - (1.39), and expressing the stress as a function of strains, we end up with

$$\begin{aligned}
\sigma_{11} &= \frac{E}{(1+\nu)(1-2\nu)}\left((1-\nu)\varepsilon_{11} + \nu\varepsilon_{22} + \nu\varepsilon_{33}\right) \\
\sigma_{22} &= \frac{E}{(1+\nu)(1-2\nu)}\left((1-\nu)\varepsilon_{22} + \nu\varepsilon_{11} + \nu\varepsilon_{33}\right) \\
\sigma_{33} &= \frac{E}{(1+\nu)(1-2\nu)}\left((1-\nu)\varepsilon_{33} + \nu\varepsilon_{11} + \nu\varepsilon_{22}\right),
\end{aligned}$$

which is valid as long as $\nu \neq 0.5$ or $\nu \neq -1$. The shear stresses are given by

$$\begin{aligned}
\sigma_{12} &= 2G\varepsilon_{12} \\
\sigma_{23} &= 2G\varepsilon_{23} \\
\sigma_{31} &= 2G\varepsilon_{31}.
\end{aligned}$$

We follow the convention described in [17], and represent the strains and stresses as column matrices, in order to conveniently express the stress-strain relationship. Using this notation, we have

$$\boldsymbol{\sigma} = \begin{bmatrix} \sigma_{11} \\ \sigma_{22} \\ \sigma_{33} \\ \sigma_{23} \\ \sigma_{31} \\ \sigma_{12} \end{bmatrix}, \quad \boldsymbol{\varepsilon} = \begin{bmatrix} \varepsilon_{11} \\ \varepsilon_{22} \\ \varepsilon_{33} \\ 2\varepsilon_{23} \\ 2\varepsilon_{31} \\ 2\varepsilon_{12} \end{bmatrix}.$$

Finally we can express the stress-strain relationship, called the generalized Hooke's law, as

$$\boldsymbol{\sigma} = \mathfrak{C}\boldsymbol{\varepsilon}, \tag{1.40}$$

where $\mathfrak{C}$ is a fourth-order tensor called the stiffness tensor, defined as

$$\mathfrak{C} = \frac{E}{1+\nu}\begin{bmatrix} \frac{1-\nu}{1-2\nu} & \frac{\nu}{1-2\nu} & \frac{\nu}{1-2\nu} & 0 & 0 & 0 \\ \frac{\nu}{1-2\nu} & \frac{1-\nu}{1-2\nu} & \frac{\nu}{1-2\nu} & 0 & 0 & 0 \\ \frac{\nu}{1-2\nu} & \frac{\nu}{1-2\nu} & \frac{1-\nu}{1-2\nu} & 0 & 0 & 0 \\ 0 & 0 & 0 & \frac{1}{2} & 0 & 0 \\ 0 & 0 & 0 & 0 & \frac{1}{2} & 0 \\ 0 & 0 & 0 & 0 & 0 & \frac{1}{2} \end{bmatrix}. \tag{1.41}$$

1.2.5 Governing equations of linear elasticity

The principle of conservation of linear momentum, which is based on Newton's second law, states that the rate of change of the linear momentum of an arbitrary part of a continuous medium is equal to the resultant force acting on that part [21]. The resultant force is the sum of body forces $\boldsymbol{f}$ and surface forces $\boldsymbol{T} = \boldsymbol{\sigma} \cdot \boldsymbol{n}$. Integrating the sum of these forces over a volume gives us Cauchy's momentum equation

$$\rho \frac{D\boldsymbol{v}}{Dt} = \nabla \cdot \boldsymbol{\sigma} + \boldsymbol{f}, \tag{1.42}$$

where ρ is the density. If we assume the body has negligible acceleration, we can set $\frac{D\boldsymbol{v}}{Dt} = 0$, which corresponds to the equilibrium equations. We can now present the governing equations of linear elasticity:

- Equilibrium equations
  $\nabla \cdot \boldsymbol{\sigma} + \boldsymbol{f} = 0$
- Stress-strain relationship
  $\boldsymbol{\sigma} = \mathfrak{C}\boldsymbol{\varepsilon}$
- Strain-displacement relationship
  $\boldsymbol{\varepsilon} = \frac{1}{2}\left(\nabla \boldsymbol{u} + (\nabla \boldsymbol{u})^T\right)$

The stress-strain relationship is dependent on the material, and for isotropic materials, the stress-strain relationship is given by

$$\boldsymbol{\sigma} = 2\mu\boldsymbol{\varepsilon} + \lambda(tr(\boldsymbol{\varepsilon}))\boldsymbol{I} = 2\mu\boldsymbol{\varepsilon}(\boldsymbol{u}) + \lambda\left(\nabla \cdot \boldsymbol{u}\right)\boldsymbol{I}, \tag{1.43}$$

where λ and μ are the first and second Lamé parameter respectively, and $tr(\cdot)$ is the trace function. The first Lamé parameter λ is related to resistance to compression, and the second parameter μ represents resistance to shear strain. In general, the parameters can be spatially varying, i.e. $\lambda(\boldsymbol{x})$ and $\mu(\boldsymbol{x})$.

We can insert the stress-strain and strain-displacement relationship into the equilibrium equations to obtain

$$\nabla \cdot \big(2\mu\boldsymbol{\varepsilon}(\boldsymbol{u}) + \lambda(\nabla \cdot \boldsymbol{u})\boldsymbol{I}\big) + \boldsymbol{f} = 0, \tag{1.44}$$

which is often referred to as the displacement formulation, as it is formulated with $\boldsymbol{u}$ as the only unknown.

1.2.6 Navier-Lamé equations

If we now assume that the Lamé parameters are constants, equation (1.44) can be written as

$$\begin{aligned} 0 &= \sigma_{ij,i} + f_i \\ &= \mu(u_{i,ji} + u_{j,ii}) + \lambda u_{k,ki} + f_i \\ &= \mu u_{j,ii} + (\mu + \lambda)u_{j,ji} + f_i, \end{aligned} \tag{1.45}$$

or in vector form

$$\mu\nabla^2\boldsymbol{u} + (\mu + \lambda)\nabla(\nabla \cdot \boldsymbol{u}) + \boldsymbol{f} = 0, \tag{1.46}$$

where $\nabla^2 = \nabla \cdot \nabla$ is the Laplace operator. These equations are called the Naiver-Lamé equations of elasticity [20].

It is often useful to express the stress-strain relationship (1.43) with other elastic moduli, as they can be easier to interpret. Examples of such moduli are the bulk modulus K, which measures resistance to compression [22], and the previously introduced Poisson's ratio ν. The relationship to the Lamé parameters is given by

$$K = \lambda + \frac{2\mu}{3}, \qquad \nu = \frac{\lambda}{2(\lambda + \mu)}. \tag{1.47}$$

Note that the second Lamé parameter is identical to the shear modulus, often denoted by G.

1.3 Calculus of variations and energy minimization

This section gives a short overview of calculus of variations, and the Navier-Lamé equations from subsection 1.2.6 are derived using energy minimization and variational principles.

In ordinary differential calculus, if we want to find the extreme points of a function, we take the derivative and set it equal to zero. Calculus of variation is,

broadly speaking, a generalization of this approach. Instead of a function we have a functional, and the points we seek are now functions.

A functional is a mapping that transforms functions from a function space into a real number field. An integral of the form

$$I(\boldsymbol{u}) = \int_{\Omega} F(\boldsymbol{x}, \boldsymbol{u}, \nabla \boldsymbol{u})\, d\boldsymbol{x}$$

whose value is a real number, is an example of a functional. The minimum of the functional $I(\boldsymbol{u})$ involves differentiation with respect to the dependent variables. The derivative with respect to a dependent variable is know as the Gâteaux derivative, and is defined as [20]

$$\delta F(\boldsymbol{u}; \boldsymbol{v}) = \lim_{\epsilon \to 0} \frac{1}{\epsilon} \big(F(\boldsymbol{u} + \epsilon \boldsymbol{v}) \big) = \frac{d}{d\epsilon} F(\boldsymbol{u} + \epsilon \boldsymbol{v}) \bigg|_{\epsilon=0}. \tag{1.48}$$

The operator δ is known as the variational operator, and $\delta F(\boldsymbol{u}; \boldsymbol{v})$ is the first variation of the function $F(\boldsymbol{u})$ in the direction of $\boldsymbol{v}$. The quantity $\epsilon \boldsymbol{v}$ is called the first variation of $\boldsymbol{u}$ and is denoted as $\delta \boldsymbol{u}$.

The necessary and sufficient conditions for the minimum of the functional are

$$\delta I = 0,$$
$$\delta^2 I > 0,$$

where the first is necessary and the second is sufficient [20].

1.3.1 Minimization of total potential energy

For a linearly elastic body $\mathcal{B}$, occupying volume Ω, with boundary $\partial\Omega$, the total strain energy is given by

$$U = \frac{1}{2} \int_{\Omega} \boldsymbol{\sigma} : \boldsymbol{\varepsilon}\, d\boldsymbol{x} = \frac{1}{2} \int_{\Omega} \sigma_{ij} \varepsilon_{ij}\, d\boldsymbol{x}. \tag{1.49}$$

This can be seen as the energy stored within $\mathcal{B}$ when work has been done on it. The total work done by applied body forces $\boldsymbol{f}$ and surface forces $\boldsymbol{T}$ is given by

$$V = -\left[\int_{\Omega} \boldsymbol{f} \cdot \boldsymbol{u}\, d\boldsymbol{x} + \int_{\partial\Omega} \boldsymbol{T} \cdot \boldsymbol{u}\, ds \right]. \tag{1.50}$$

The energy U is the available strain energy stored in the body, and the energy in V is expended, hence the negative sign. The total potential energy functional

$\Pi(\boldsymbol{u})$, of body $\mathcal{B}$, is the sum of the strain energy and work done by external forces

$$\Pi(\boldsymbol{u}) = U + V = \frac{1}{2}\int_\Omega \boldsymbol{\sigma} : \boldsymbol{\varepsilon}\, d\boldsymbol{x} - \left[\int_\Omega \boldsymbol{f}\cdot\boldsymbol{u}\, d\boldsymbol{x} + \int_{\partial\Omega} \boldsymbol{T}\cdot\boldsymbol{u}\, ds\right] \tag{1.51}$$

$$= \int_\Omega \left(\frac{1}{2}\boldsymbol{\sigma} : \boldsymbol{\varepsilon} - \boldsymbol{f}\cdot\boldsymbol{u}\right) d\boldsymbol{x} - \int_{\partial\Omega} \boldsymbol{T}\cdot\boldsymbol{u}\, ds. \tag{1.52}$$

Notice the dependent variable here is the displacement field $\boldsymbol{u}$. If the body is in equilibrium, then out of all admissible displacements fields $\boldsymbol{u}$, the one that minimizes the total potential energy, denoted $\boldsymbol{u}_0$, corresponds to the equilibrium solution, i.e.

$$\Pi(\boldsymbol{u}_0) \leq \Pi(\boldsymbol{u}). \tag{1.53}$$

This is the principle of minimum total potential energy [20]. An admissible displacement field is one that satisfies the geometric constraints of the problem.

1.3.2 Derivation of Naiver-Lamé equations through energy minimization

We can apply the principle of minimum potential energy to the total potential energy functional derived in the previous section to obtain the Navier-Lamé equations of elasticity.

Let us again consider a isotropic linear elastic body $\mathcal{B}$, occupying volume Ω with boundary $\partial\Omega$. The body is subjected to a body force $\boldsymbol{f}$, and traction force $\widehat{\boldsymbol{T}}$ on a portion $\partial\Omega_N$ of the surface (Neumann boundary condition). The displacement vector $\boldsymbol{u}$ is specified to be $\widehat{\boldsymbol{u}}$ on $\partial\Omega_D$ (Dirichlet boundary condition), which is the remaining portion of the boundary. Note that $\partial\Omega = \partial\Omega_N \cup \partial\Omega_D$.

From eq (1.51) we have the total potential energy of $\mathcal{B}$ given as

$$\Pi(\boldsymbol{u}) = \int_\Omega \left(\frac{1}{2}\boldsymbol{\sigma} : \boldsymbol{\varepsilon} - \boldsymbol{f}\cdot\boldsymbol{u}\right) d\boldsymbol{x} - \int_{\partial\Omega_N} \widehat{\boldsymbol{T}}\cdot\boldsymbol{u}\, ds$$

$$= \int_\Omega \left(\frac{1}{2}\sigma_{ij}\varepsilon_{ij} - f_i u_i\right) d\boldsymbol{x} - \int_{\partial\Omega_N} \widehat{T}_i u_i\, ds, \tag{1.54}$$

As $\mathcal{B}$ is linearly elastic and isotropic, we have strain-displacement relation given by (1.33), and the stress-strain relation given by (1.43). Assuming the body is homogeneous, meaning constant Lamé parameters, we can substitute these equations

into (1.54) to get

$$\Pi(\boldsymbol{u}) = \int_\Omega \left[\frac{\mu}{4} \left(u_{i,j} + u_{j,i}\right) \left(u_{i,j} + u_{j,i}\right) + \frac{\lambda}{2} u_{i,i} u_{k,k} - f_i u_i \right] d\boldsymbol{x} - \int_{\partial\Omega_N} \widehat{T}_i u_i \, ds. \tag{1.55}$$

Using the principle of minimum potential energy and setting the first variation of Π to be zero, we obtain

$$0 = \int_\Omega \left[\frac{\mu}{2} (\delta u_{i,j} + \delta u_{j,i})(u_{i,j} + u_{j,i}) + \lambda \delta u_{i,i} u_{k,k} - f_i \delta u_i \right] d\boldsymbol{x} - \int_{\partial\Omega_N} \widehat{T}_i \delta u_i \, ds. \tag{1.56}$$

Here we have used the product rule of variation and combined terms. We want to set the coefficient of δu_i to zero, but first we need to relieve it of any derivatives. To do so, we use integration-by-parts, which can be expressed as follows

$$\int_\Omega \delta u_{i,j} (u_{i,j} + u_{j,i}) \, d\boldsymbol{x} = \int_{\partial\Omega} \delta u_i (u_{i,j} \; u_{j,i}) n_j \, ds - \int_\Omega \delta u_i (u_{i,j} + u_{j,i})_{,j} \, d\boldsymbol{x},$$

where n_j is the outward unit vector in the jth direction. Using this in equation (1.56) we get

$$\begin{aligned} 0 &= \int_\Omega \left[-\frac{\mu}{2} (u_{i,j} + u_{j,i})_{,j} \delta u_i - \frac{\mu}{2} (u_{i,j} + u_{j,i})_{,i} \delta u_j - \lambda u_{k,ki} \delta u_i - f_i \delta u_i \right] d\boldsymbol{x} \\ &\quad + \int_{\partial\Omega} \left[\frac{\mu}{2} (u_{i,j} + u_{j,i})(n_j \delta u_i + n_i \delta u_j) + \lambda u_{k,k} n_i \delta u_i \right] ds - \int_{\partial\Omega_N} \delta u_i \widehat{T}_i \, ds \\ &= \int_\Omega \left[-\mu (u_{i,j} + u_{j,i})_{,j} - \lambda u_{k,ki} - f_i \right] \delta u_i d\boldsymbol{x} \\ &\quad + \int_{\partial\Omega} \left[\mu (u_{i,j} + u_{j,i}) + \lambda u_{k,k} \delta_{ij} \right] n_j \delta u_i \, ds - \int_{\partial\Omega_N} \delta u_i \widehat{T}_i \, ds. \end{aligned} \tag{1.57}$$

Next we note that $\mu(u_{i,j} + u_{j,i}) + \lambda u_{k,k} \delta_{ij} = \sigma_{ij}$ and by the Cauchy stress formula we have $\sigma_{ij} n_j = T_i$. Therefore the first surface integral in (1.57) can be rewritten as

$$\int_{\partial\Omega} \left[\mu (u_{i,j} + u_{j,i}) + \lambda u_{k,k} \delta_{ij} \right] n_j \delta u_i \, ds = \int_{\partial\Omega} T_i \delta u_i \, ds.$$

Further, we can split this surface integral to obtain

$$\int_{\partial\Omega} T_i \delta u_i \, ds = \int_{\partial\Omega_N} T_i \delta u_i \, ds + \int_{\partial\Omega_D} T_i \delta u_i \, ds = \int_{\partial\Omega_N} T_i \delta u_i \, ds.$$

Notice that the surface integral over $\partial\Omega_D$ was set to zero as u_i is specified there, meaning we have $\delta u_i = 0$. Inserting this into (1.57), we are left with

$$0 = \int_\Omega \left[-\mu(u_{i,j} + u_{j,i})_{,j} - \lambda u_{k,ki} - f_i\right] \delta u_i \, d\boldsymbol{x} + \int_{\partial\Omega_N} \delta u_i (T_i - \widehat{T}_i) \, ds. \tag{1.58}$$

Finally we use the fundamental lemma of calculus of variations and set the coefficients of δu_i in Ω and $\partial\Omega_N$ to zero separately, and obtain

$$\begin{aligned} \mu u_{i,jj} + (\mu + \lambda) u_{k,ki} \; f_i = 0 \quad &\text{in} \quad \Omega \\ u_i - \widehat{u}_i = 0 \quad &\text{on} \quad \partial\Omega_D \\ T_i - \widehat{T}_i = 0 \quad &\text{on} \quad \partial\Omega_N \end{aligned}$$

or in vector form

$$\begin{aligned} \mu\nabla^2 \boldsymbol{u} + (\mu + \lambda)\nabla(\nabla \cdot \boldsymbol{u}) + \boldsymbol{f} = 0 \quad &\text{in} \quad \Omega \\ \boldsymbol{u} - \widehat{\boldsymbol{u}} = 0 \quad &\text{on} \quad \partial\Omega_D \\ \boldsymbol{T} - \widehat{\boldsymbol{T}} = 0 \quad &\text{on} \quad \partial\Omega_N \end{aligned} \tag{1.59}$$

Equations (1.59) are the familiar Navier-Lamé equations with boundary conditions.

1.4 Numerical methods

In this section, we give an overview of the numerical methods used in this thesis. Quasi-Newton methods are needed to efficiently solve the optimization problems arising in image registration, and the multi-point stress approximation will be used to robustly solve the equations of elasticity.

1.4.1 Quasi-Newton methods

Quasi-Newton methods are a family of optimization methods used to find maxima and minima of functions, and are based on Newtons method. They approximate the Hessian matrix in order to avoid some of the disadvantages with the regular Newton method. Two quasi-Newton methods will be discussed here, the BFGS and Gauss-Newton method, as they will be used to efficiently solve the minimization problems found in image registration.

We start by introducing Newtons method for optimization. Given a twice differentiable function $f : \mathbb{R}^n \to \mathbb{R}$, dependent on $\boldsymbol{x} = [x_1, x_2, \ldots, x_n]$, we want to solve the minimization problem

$$\min_{\boldsymbol{x} \in \mathbb{R}^n} \quad f(\boldsymbol{x}). \tag{1.60}$$

The second-order Taylor expansion of f around an iterate $\boldsymbol{x}_k$ is given by

$$f(\boldsymbol{x}_k + \boldsymbol{p}) \approx f(\boldsymbol{x}_k) + \nabla f(\boldsymbol{x}_k)^T \boldsymbol{p} + \frac{1}{2} \boldsymbol{p}^T H_f(\boldsymbol{x}_k) \boldsymbol{p}, \tag{1.61}$$

where $\boldsymbol{p}$ is the search direction, and $H_f(\boldsymbol{x})$ is the Hessian matrix of f at point $\boldsymbol{x}$. The minimum of $f(\boldsymbol{x}_k + \boldsymbol{p})$ in $\boldsymbol{p}$ can give us a new direction towards $\boldsymbol{x}^*$ which minimizes f. This is given by the solution of

$$\nabla f(\boldsymbol{x}_k + \boldsymbol{p}) = \nabla f(\boldsymbol{x}_k) + H_f(\boldsymbol{x}_k) \boldsymbol{p} = 0 \tag{1.62}$$

with respect to $\boldsymbol{p}$. We solve for $\boldsymbol{p}$ to get an expression for the search direction

$$\boldsymbol{p} = -H_f^{-1}(\boldsymbol{x_k}) \nabla f(\boldsymbol{x_k}). \tag{1.63}$$

Finally, we can define Newtons method as

$$\boldsymbol{x}_{k+1} = \boldsymbol{x}_k - H_f^{-1}(\boldsymbol{x}_k) \nabla f(\boldsymbol{x}_k). \tag{1.64}$$

There are several issues with Newtons method. Firstly, the Hessian matrix needs to be positive-definite to guarantee the existence of its inverse, and as a consequence the existence of the search direction (1.63). Even when it does exits, it is not guaranteed to satisfy the decent property $\nabla f(\boldsymbol{x_k})^T \boldsymbol{p} < 0$ [23]. Secondly, the computation of the Hessian matrix is often a costly procedure in terms of computational power.

BFGS

Quasi-Newton methods are designed to approximate the Hessian matrix instead of computing it at every iteration. The approximations are often done in a way to avoid problems with non-positive-definite and non-invertible Hessian matrices [24].

The approximated Hessian matrix $B_f(\boldsymbol{x}_k)$ is updated at every iteration to incorporate new information about the curvature. It is required to satisfy the so called secant equation [23]

$$B_f(\boldsymbol{x}_{k+1}) \boldsymbol{s}_k = \boldsymbol{y}_k, \tag{1.65}$$

where

$$\boldsymbol{s_k} = \boldsymbol{x}_{k+1} - \boldsymbol{x}_k, \qquad \boldsymbol{y}_k = \nabla f(\boldsymbol{x}_{k+1}) - \nabla f(\boldsymbol{x}_k).$$

Several popular Hessian approximation exits, however, we only note the Broyden-Fletcher-Goldfarb-Shanno (BFGS) method as it will be the one used in this thesis. The BFGS update formula is given by

$$B_f(\boldsymbol{x}_{k+1}) = B_f(\boldsymbol{x}_k) + \frac{\boldsymbol{y}_k \boldsymbol{y}_k^T}{\boldsymbol{y}_k^T \boldsymbol{s}_k} - \frac{B_f(\boldsymbol{x}_k)\boldsymbol{s}_k \boldsymbol{s}_k^T B_f(\boldsymbol{x}_k)}{\boldsymbol{s}_k^T B_f(\boldsymbol{x}_k)\boldsymbol{s}_k}, \tag{1.66}$$

and the iterative formula for updating $\boldsymbol{x}_k$ is given by

$$\boldsymbol{x}_{k+1} = \boldsymbol{x}_k - \gamma_k B_f(\boldsymbol{x}_k)^{-1} \nabla f(\boldsymbol{x}_k), \tag{1.67}$$

where γ_k modifies the step-length to ensure sufficient decrease of the objective function through a line-search. See e.g. *Numerical Optimization* by Jorge Nocedal for a more detailed discussion [23].

Gauss-Newton

In the case of the minimization problem being a least-square problem, we can exploit certain characteristics to efficiently search for the minimum. We now assume f in equation (1.60) can be expressed as

$$f(\boldsymbol{x}) = \frac{1}{2} \sum_{i=1}^{m} \big(q_i(\boldsymbol{x})\big)^2 = \frac{1}{2} \boldsymbol{q}(\boldsymbol{x})^T \boldsymbol{q}(\boldsymbol{x}), \tag{1.68}$$

where $\boldsymbol{q} : \mathbb{R}^n \to \mathbb{R}^m$, with $m \geq n$. The Jacobian matrix of $\boldsymbol{q}$ is given as

$$\boldsymbol{J}_{\boldsymbol{q}}(\boldsymbol{x}) = \begin{bmatrix} \nabla q_1(\boldsymbol{x})^T \\ \vdots \\ \nabla q_m(\boldsymbol{x})^T \end{bmatrix},$$

and the by the chain rule we have the gradient of $f(\boldsymbol{x})$

$$\nabla f(\boldsymbol{x}) = \sum_{i=1}^{m} q_i(\boldsymbol{x}) \nabla q_i(\boldsymbol{x}) = \boldsymbol{J}_{\boldsymbol{q}}(\boldsymbol{x})^T \boldsymbol{q}(\boldsymbol{x}) \tag{1.69}$$

Further, the Hessian matrix is given by

$$H_f(\boldsymbol{x}) = \boldsymbol{J}_{\boldsymbol{q}}(\boldsymbol{x})^T \boldsymbol{J}_{\boldsymbol{q}}(\boldsymbol{x}) + \sum_{i=1}^{m} q_i(\boldsymbol{x}) H_{q_i}(\boldsymbol{x}). \tag{1.70}$$

The defining characteristic of the Gauss-Newton method is that it approximates the Hessian matrix by neglecting the last term in (1.70), leaving us with the Gauss-Newton iterative scheme

$$\boldsymbol{x}_{k+1} = \boldsymbol{x}_k - \gamma_k \Big(\boldsymbol{J}_{\boldsymbol{q}}(\boldsymbol{x}_k)^T \boldsymbol{J}_{\boldsymbol{q}}(\boldsymbol{x}_k)\Big)^{-1} \boldsymbol{J}_{\boldsymbol{q}}(\boldsymbol{x}_k)^T \boldsymbol{q}(\boldsymbol{x}_k). \tag{1.71}$$

The Gauss-Newton scheme is favorable for minimizing least square problems as it only requires the calculation of the Jacobian of $\boldsymbol{q}$. Further, if $\boldsymbol{J}_{\boldsymbol{q}}$ has full rank, the direction calculated is guaranteed to be a decent direction [23].

1.4.2 Multi-point stress approximation

The multi-point stress approximation (MPSA) is an an extension to the well established multi-point flux approximation (MPFA) developed for flow simulations in porous media [25]. It is a cell-centered finite volume method that solves vector variable problems, in our case Hooke's law for linearly elastic materials where we solve for the displacement. The method is particularly favorable for its ability to handle heterogeneous and discontinuous coefficients, which will be important to us when we solve the elasticity equations with heterogeneous Lamé parameters. This section is based on *Cell-centered finite volume discretizations for deformable porous media* by Nordbotten [26].

Let Ω be some domain with boundary $\partial\Omega$. The static momentum balance equations for an elastic medium reads

$$\int_{\partial\Omega} \boldsymbol{T}\, dA + \int_{\Omega} \boldsymbol{f}\, dV = 0, \tag{1.72}$$

where $\boldsymbol{T}$ are the surface traction vectors on the boundary, and $\boldsymbol{f}$ are the body forces acting in the material. Recall that in the case of small deformations and a linear stress-strain relationship, we have the Cauchy stress formula

$$\boldsymbol{T} = \boldsymbol{\sigma} \cdot \boldsymbol{n}, \tag{1.73}$$

where $\boldsymbol{\sigma}$ is the Cauchy stress tensor, and $\boldsymbol{n}$ is the outward facing normal vector. Equation (1.72) and (1.73) can be rewritten into the equilibrium equations

$$\nabla \cdot \boldsymbol{\sigma} + \boldsymbol{f} = 0. \tag{1.74}$$

Discrete momentum conservation

We partition our domain into non-overlapping cells Ω_i. For two cells Ω_i and Ω_j, denote their shared boundary $e_{i,j}$, called a cell face. We can now rewrite (1.72) for each cell as

$$\sum_j \int_{e_{i,j}} \boldsymbol{T}\, dA + \int_{\Omega_i} \boldsymbol{f}\, dV = 0. \tag{1.75}$$

Let $\boldsymbol{f}_i$ be the volume average force over the cell Ω_i and $\boldsymbol{T}_{i,j}$ the surface average stress over face $e_{i,j}$. This subscript notation must not be confused with Einstein notation. Using this notation, (1.75) can be written as

$$\frac{1}{|\Omega_i|} \sum_j \left|e_{i,j}\right| \boldsymbol{T}_{i,j} + \boldsymbol{f}_i = 0 \tag{1.76}$$

Discrete stress

The finite volume method is completed through the choice of a discrete expression for the stress on cell faces. This is where Hooke's law comes in. We want to express the surface stress $\boldsymbol{T}_{i,j}$ as a linear function of the displacement $\boldsymbol{u}_i$. For the conservation property in (1.75) to be fulfilled, we must require that $\boldsymbol{T}_{i,j} = -\boldsymbol{T}_{j,i}$, where for each face we linearly approximate the traction vector as

$$\boldsymbol{T}_{i,j} = \sum_k t_{i,j,k} \boldsymbol{u}_k, \tag{1.77}$$

where $t_{i,j,k} = -t_{j,i,k}$ are called the stress weight tensors, and k denote cells neighboring the edge $e_{i,j}$.

The calculation of $t_{i,j,k}$ for face $e_{i,j}$ is split into smaller calculations by using a dual grid that divides the faces into subfaces, see Figure 1.7. The volume associated with corner l and cell Ω_i we call a subcell and is denoted $\widetilde{\Omega}_{i,l}$. Further, we have subfacecs denoted $\widetilde{e}_{i,j,l}$, and stress weights for subface $\widetilde{e}_{i,j,l}$ are denoted $\widetilde{t}_{i,j,l,k}$, and we have

$$t_{i,j,k} = \sum_l \widetilde{t}_{i,j,l,k}. \tag{1.78}$$

Given a corner l, the number of subcells to consider when calculating the stress weight tensor for each subface will depend on the type of MPSA method used. The most popular being the O, L, and U-method.

Calculation of stress weights

To calculate the stress weights for each subface, we first need to define the displacement within each subcell. To do so, consider a linear approximation of the stress weights for subface $\widetilde{e}_{i,j,l}$ to the displacement within each subcell $\widetilde{\Omega}_{i,l}$, which is then approximated by a multi-linear function of the spacial coordinates

$$\boldsymbol{u} = \boldsymbol{u}_i + \nabla \boldsymbol{u}_{i,l} \cdot (\boldsymbol{x} - \boldsymbol{x_i}) \quad \text{for} \quad \boldsymbol{x}_i \in \widetilde{\Omega}_{i,l}, \tag{1.79}$$

where $\nabla \boldsymbol{u}_{i,l}$ is the gradient of the displacement within $\widetilde{\Omega}_{i,l}$.

We now impose continuity requirements for the traction and displacement. Traction continuity over a subface is given by

$$\boldsymbol{T}_{i,j,k} = -\boldsymbol{T}_{j,i,k}. \tag{1.80}$$

Remembering that $\boldsymbol{T} = \boldsymbol{\sigma} \cdot \boldsymbol{n}$, we can write it as

$$\left[\mathfrak{C}_i : \left(\nabla \boldsymbol{u}_{i,l} + \left(\nabla \boldsymbol{u}_{i,l}\right)^T\right)\right] \cdot \boldsymbol{n}_{i,m,l} = \left[\mathfrak{C}_j : \left(\nabla \boldsymbol{u}_{j,l} + \left(\nabla \boldsymbol{u}_{j,l}\right)^T\right)\right] \cdot \boldsymbol{n}_{i,m,l} \quad \text{if} \quad \widetilde{e}_{i,m,l} \subset \widetilde{e}_{i,j,l},$$

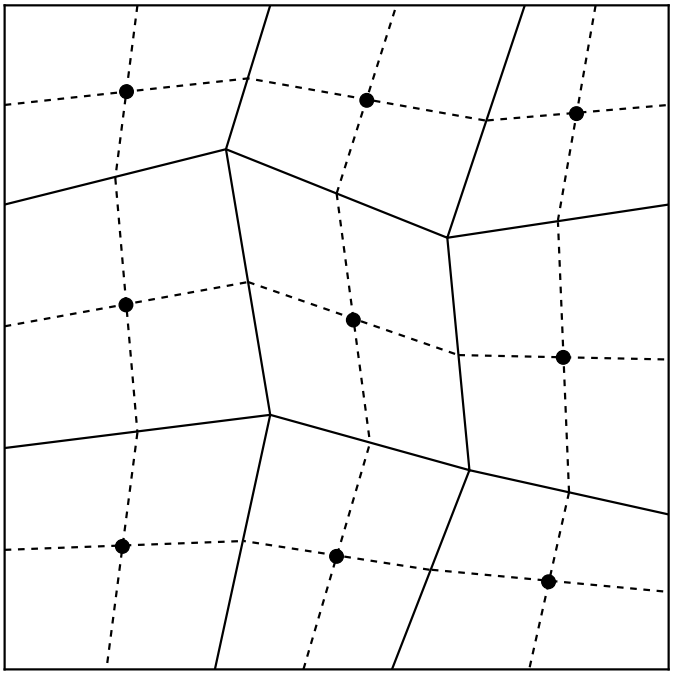

Figure 1.7: Visualization of grid with solid black lines, and the dual grid with dashed lines. Cell centers are marked by dots. Note that the grid is shown as non-orthogonal to highlight the capabilities of the MPSA method, however, we use orthogonal girds in all our experiments. Figure is adapted from [26].

where $\boldsymbol{n}_{i,m,l}$ is the average normal vector of subface $\widetilde{e}_{i,m,l}$.

Displacement continuity is given by

$$\boldsymbol{u}_i + \nabla \boldsymbol{u}_{i,l} \cdot (\widetilde{\boldsymbol{x}}_{i,m,l,n} - \boldsymbol{x}_i) = \boldsymbol{u}_j + \nabla \boldsymbol{u}_{j,l} \cdot (\widetilde{\boldsymbol{x}}_{i,m,l,n} - \boldsymbol{x}_j), \tag{1.81}$$

where $\widetilde{\boldsymbol{x}}_{i,m,l,n}$ is called a continuity point.

Finally, one can now assemble linear system for the unknown gradients $\nabla \boldsymbol{u}_{i,l}$ within the interaction regions. Once we have the gradients, we can calculate the local stresses from the constitutive relation and finally the traction vector for each face and cell-centered displacement.

Chapter 2

Elastic Image Registration

In this chapter, traditional elastic registration is derived through the use of fundamental concepts from linear elasticity and energy minimization. The arising image-derived forces are discussed, along with some disadvantages of the method. Then, a novel elastic registration method presented and discussed. Implementation details of both methods are covered.

2.1 Traditional elastic image registration

The elastic registration method assumes that the image subject behaves linearly elastic, and intends to regularize the problem such that the resulting displacement field conforms with this assumption. It is widely used in medical imaging, as the linear elastic model can be used to model tissue and organs. Registration is often required as changes in the anatomy during the imaging process is a normal, and often unavoidable occurrence. These changes can, for example, come as a result of patient movement, respiration, or the heart beating.

Elastic registration is now derived using fundamentals from linear elasticity and principals of energy minimization. Recall from subsection 1.3.1 that the total potential energy for a body is given by the functional

$$\Pi = U + V, \tag{2.1}$$

where U is the strain energy, defined as the energy stored in the body due to some deformation, and V is work done by external forces. If the body is linearly elastic, the strain energy is given by

$$U = \frac{1}{2} \int_{\Omega} \boldsymbol{\sigma} : \boldsymbol{\varepsilon} \, d\boldsymbol{x}. \tag{2.2}$$

Further, if the body it is isotropic, we have the familiar stress-strain and strain-displacement relations

$$\boldsymbol{\sigma} = 2\mu\boldsymbol{\varepsilon} + \lambda tr(\boldsymbol{\varepsilon})\boldsymbol{I}, \quad \text{and} \quad \boldsymbol{\varepsilon} = \frac{1}{2}\left(\nabla \boldsymbol{u} + (\nabla \boldsymbol{u})^T\right),$$

which we can insert into (2.2) to get

$$U = \frac{1}{2}\int_\Omega \boldsymbol{\sigma} : \boldsymbol{\varepsilon}\, d\boldsymbol{x} = \int_\Omega \frac{\mu}{4}\left(u_{i,j} + u_{j,i}\right)\left(u_{i,j} + u_{j,i}\right) + \frac{\lambda}{2}u_{i,i}u_{k,k}\, d\boldsymbol{x}. \tag{2.3}$$

We can recognize the above equation as the elastic regularizer first introduced in subsection 1.1.4. Elastic registration mimics the functional Π from (2.1) by using a distance measure $\mathcal{D}$ to model the work done by external forces V. This is added to the physical measure of strain energy U, giving us the defining functional for elastic registration

$$\mathcal{J}(\boldsymbol{u}) = \mathcal{D}(\mathcal{T}_{\boldsymbol{u}}, \mathcal{R}) + \alpha \int_\Omega \frac{\mu}{4}\left(u_{i,j} + u_{j,i}\right)\left(u_{i,j} + u_{j,i}\right) + \frac{\lambda}{2}u_{i,i}u_{k,k}\, d\boldsymbol{x}, \tag{2.4}$$

where $\mathcal{T}_{\boldsymbol{u}}$ and $\mathcal{R}$ are the transformed moving image and reference image respectively, and α is the regularization parameter. By the principle of minimum potential energy, the problem is now to find the displacement field $\boldsymbol{u}$ which minimizes $\mathcal{J}(\boldsymbol{u})$. In other words, elastic registration is defined by the following minimization problem

$$\min_{\boldsymbol{u}} \quad \mathcal{J}(\boldsymbol{u}), \tag{2.5}$$

which we from now on refer to as the traditional elastic registration method, to differentiate it from the elastic method to be derived later in this chapter.

2.1.1 Solution strategies

To solve (2.5), one has to choose between the so called discretize-then-optimize (DTO) approach, and the optimize-then-discretize (OTD) approach. With the DOP approach, the minimization problem is directly discretized to obtain a high dimensional nonlinear optimization problem, which is then typically solved with an iterative solver [27, 3].

The OTD approach solves the problem using variational principles. It begins by finding the necessary continuous optimality conditions analytically, known as the Euler-Lagrange equations, and then optimizes the equivalent system [6]. In other words, we find the stationary points of the equations. The optimality conditions are found by using calculus of variation and calculating the first variation, or the Gâteaux derivative, of $\mathcal{J}(\boldsymbol{u})$. The derivation is analogous to the one done

in subsection 1.3.2. This results in the Euler-Lagrange equations, which for the traditional elastic registration problem becomes [6]

$$\begin{cases} \boldsymbol{f}_{IR}(\boldsymbol{x}, \boldsymbol{u}) + \alpha \left(\mu \nabla^2 \boldsymbol{u} + (\lambda + \mu) \nabla (\nabla \cdot \boldsymbol{u}) \right) = 0 & \text{in} \quad \Omega \\ \boldsymbol{\sigma} \cdot \boldsymbol{n} = 0 & \text{on} \quad \partial\Omega \end{cases} \tag{2.6}$$

where $\boldsymbol{f}_{IR}(\boldsymbol{x}, \boldsymbol{u}(\boldsymbol{x}))$ is the Gâteaux derivative of the distance functional. We recognize (2.6) as the Navier-Lamé equations. The homogeneous Neumann boundary conditions are the natural conditions arising when deriving the Euler-Lagrange equations, which must be satisfied when no condition is prescribed on the boundary (see e.g. [6] for a more detailed discussion). The equations would now be discretized and solved for $\boldsymbol{u}$, typically with either a fixed-point iteration method, or by introducing an artificial time variable and determining the steady-state solution of the system.

2.1.2 Image-derived forces

In equation (2.6), we see the appearance of $\boldsymbol{f}_{IR}(\boldsymbol{x}, \boldsymbol{u})$, and if we were to use the terminology from subsection 1.3.1, it would be natural to view this as a force acting on the body. Lets call $\boldsymbol{f}_{IR}(\boldsymbol{x}, \boldsymbol{u})$ the *image force*, and notice that it is dependent on both $\boldsymbol{x}$ and $\boldsymbol{u}$, meaning it is a nonlinear term. It can be viewed as an external force that pushes every individual point in the moving image in a specific direction, in order to minimizes the distance measure. The regularizing term can be viewed as internal forces resisting this displacement until an equilibrium state is found.

As previously stated, the image force is the Gâteaux derivative of the distance functional. If $\mathcal{D} = \mathcal{D}^{SSD}$ is chosen as the distance measure, the image force becomes [6]

$$\boldsymbol{f}_{IR}(\boldsymbol{x}, \boldsymbol{u}) = (\mathcal{T}_{\boldsymbol{u}} - \mathcal{R}) \nabla \mathcal{T}_{\boldsymbol{u}}. \tag{2.7}$$

Clearly, the image force is an unphysical force. No matter what distance measure is chosen, the image force will always be computed from image data alone. If the regularization parameter α is chosen to be too small, the image force will start to fit noise. If we were to a use a different distance measure, e.g. the NGF from (1.6), we would get a different expression for the image force, which would in turn act differently on the body. The force will be non-zero at locations where there is a measurable difference between the moving and reference image, and zero in areas with constant intensities.

2.1.3 Disadvantages of the traditional method

The traditional elastic image registration approach will often produce satisfactory results, however, it has several intimidate disadvantages: It relies solely on the

unphysical image force to "drive" the registration forward, as made clear by the previous section. As a consequence, the parameters μ and λ loses most of its original physical meaning, and is often refereed to as "regularization parameters" in image registration literature, as opposed to "material/tissue parameters". The process of finding a displacement field is often reduced to manually tuning the parameters α, μ, and λ so that the resulting transformed image is visually acceptable, while making sure the displacement field is physically possible, e.g. avoiding folding of the tissue. There is no unified way of choosing the regularization parameters, and the order of magnitude can greatly change based on which distance measure is chosen. Further, as the traditional elastic method solves the Navier-Lamé equations, the Lamé parameters are assumed to be constants for the entire domain, which means that assigning different parameters to different regions of the image is not possible with this method.

Equation (2.4) is essentially a sum of a physical measure of the strain energy, and an unphysical measure of the applied forces. This can be troublesome when image registration is applied to problems where the goal is to recover an appropriate approximation of the underlying displacement field. Examples of such studies can be found in [5, 28], where they conclude that one cannot expect to restore a physically correct displacement field with traditional elastic registration.

2.2 Boundary-driven elastic image registration

In many cases, the elastic deformation of a body is due to an applied force on the boundary, rather than a body force. This is not possible to model with the traditional approach due to unphysical image force and the other previously mentioned disadvantages. We now present a novel image registration method where the image force is avoided.

Let us first recall the equilibrium equations for a linearly elastic isotropic body with domain Ω, and boundary $\partial\Omega = \partial\Omega_U \cup \partial\Omega_N$,

$$\begin{cases} \boldsymbol{f}_b(\boldsymbol{x}) + \nabla \cdot \big(2\mu\boldsymbol{\varepsilon}(\boldsymbol{u}) + \lambda(\nabla \cdot \boldsymbol{u})\boldsymbol{I}\big) = 0 & \text{in} \quad \Omega, \\ \boldsymbol{u} = \boldsymbol{g}_D & \text{on} \quad \Omega_D, \\ \boldsymbol{\sigma} \cdot \boldsymbol{n} = \boldsymbol{g}_N & \text{on} \quad \Omega_N, \end{cases} \tag{2.8}$$

where $\boldsymbol{u}(\boldsymbol{x})$ is the displacement, $\boldsymbol{\sigma} = 2\mu\boldsymbol{\varepsilon} + \lambda tr(\boldsymbol{\varepsilon})\boldsymbol{I}$ is the stress tensor, $\boldsymbol{f}_b(\boldsymbol{x})$ is the body force, $\lambda(\boldsymbol{x})$ and $\mu(\boldsymbol{x})$ are the first and second Lamé parameters respectively, $\boldsymbol{g}_D$ and $\boldsymbol{g}_N$ are boundary conditions on parts of the boundary where Dirichlet and Neumann conditions are assigned respectively, and $\boldsymbol{n}$ is the outward normal vector.

Given a body force and boundary conditions, we can solve (2.8) for the displacement field $\boldsymbol{u}$. However, the actual boundary conditions are in most cases unknown,

and this is what the our new method, which we will call boundary-driven image registration (BDIR), will search for. To do so, we propose the following PDE constrained minimization problem

$$\begin{aligned} \min_{\boldsymbol{p}} \quad & \mathcal{D}\left(\mathcal{T}_{\boldsymbol{u}}, \mathcal{R}\right) \\ \text{s.t.} \quad & \boldsymbol{f}_b(\boldsymbol{x}) + \nabla \cdot \left(2\mu\boldsymbol{\varepsilon}(\boldsymbol{u}) + \lambda(\nabla \cdot \boldsymbol{u})\boldsymbol{I}\right) = 0 \quad \text{in} \quad \Omega, \\ & \qquad\qquad \boldsymbol{u} = \boldsymbol{g}_D(\boldsymbol{x}; \boldsymbol{p}) \quad \text{on} \quad \partial\Omega_D, \\ & \qquad\qquad \boldsymbol{\sigma} \cdot \boldsymbol{n} = \boldsymbol{g}_N(\boldsymbol{x}; \boldsymbol{p}) \quad \text{on} \quad \partial\Omega_N, \end{aligned} \tag{2.9}$$

where the variable we are minimizing over, $\boldsymbol{p}$, is present in the cost function implicitly through $\boldsymbol{u}$ on the boundary. $\mathcal{T}_{\boldsymbol{u}}$ and $\mathcal{R}$ are the transformed moving image and reference image respectively. $\boldsymbol{g}_D(\boldsymbol{x}; \boldsymbol{p})$ and $\boldsymbol{g}_N(\boldsymbol{x}; \boldsymbol{p})$ should be interpreted as functions defined by the parameter $\boldsymbol{p}$ and gives a value for every $\boldsymbol{x} \in \Omega_D$ and $\boldsymbol{x} \in \Omega_N$ respectively.

The PDE in the first constraint in (2.9), i.e. the equilibrium equation, is purposely kept in its most general form to avoid needing to make assumptions about μ and λ. This means the BDIR method will be able handle heterogeneous Lamé parameters, which opens up the possibility of optimizing over them, as will be done in section 3.3.

If we were to assume μ and λ are constants in Ω, the BDIR problem can be written as

$$\begin{aligned} \min_{\boldsymbol{p}} \quad & \mathcal{D}(\mathcal{T}_{\boldsymbol{u}}, \mathcal{R}) \\ \text{s.t.} \quad & \boldsymbol{f}_b(\boldsymbol{x}) + \mu\nabla^2\boldsymbol{u} + (\mu + \lambda)\nabla(\nabla \cdot \boldsymbol{u}) = 0 \quad \text{in} \quad \Omega, \\ & \qquad\qquad \boldsymbol{u} = \boldsymbol{g}_D(\boldsymbol{x}; \boldsymbol{p}) \quad \text{on} \quad \partial\Omega_D, \\ & \qquad\qquad \boldsymbol{\sigma} \cdot \boldsymbol{n} = \boldsymbol{g}_N(\boldsymbol{x}; \boldsymbol{p}) \quad \text{on} \quad \partial\Omega_N, \end{aligned} \tag{2.10}$$

where the first constraint is now the Navier-Lamé equations. There is a clear similarity between the above minimization problem and the traditional elastic image registration equation in (2.6). However, notice the important difference in the body force term. In equations (2.9) and (2.10), $\boldsymbol{f}_b(\boldsymbol{x})$ should be interpreted as the physical body force acting on the body. Typically, this is a gravitational force acting on the entire domain. This is in contrast to the previously described nonlinear image force $\boldsymbol{f}_{IR}(\boldsymbol{x}, \boldsymbol{u})$ in (2.6), which has no physical meaning. Note also that there is no longer a registration parameter α needed, as we are not balancing similarity and regularity as in the traditional case.

The BDIR method is designed for registration problems where the underlying deformation comes as a result of a force and/or displacement on the boundary. The resulting displacement field will satisfy the momentum balance equation without the need for an unphysical image force.

2.3 Implementation

The traditional elastic registration problem and the elastic BDIR problem are fundamentally different, so the implementation of the two methods will naturally differ. Implementation details for both problems are explained in is this section.

The traditional elastic registration problem is solved using the Flexible Algorithms for Image Registration (FAIR) toolbox for MATLAB [3]. As the minimization problem in (2.5) can be formulated as a least squares problem, a Gauss-Newton optimization method, described in subsection 1.4.1, with an Armijo line-search, used to minimize the problem. This means the computation of the Hessian matrix can be done with a relatively low computational cost.

A multilevel approach is used, where the images are represented through several levels of coarseness. The coarsest level is registered first, and the result is used as an initial guess for the next level. This is done to decrease the chances of the solver being stuck at a local minimum, and fewer computations is need on the finer, more expensive levels to converge.

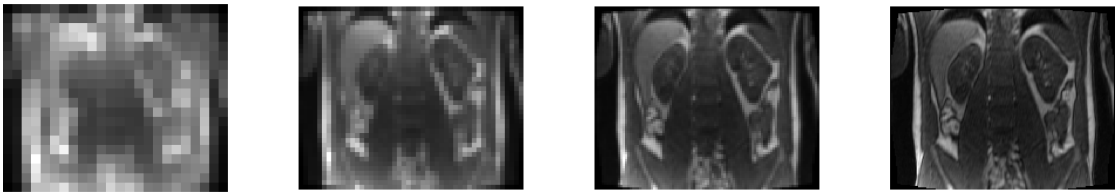

Figure 2.1: Multilevel representation of an image. Registration of the coarsest image is performed first, and its solution is used a a starting guess for the finer level.

The BDIR procedure can summarized in three steps: First, given a set of boundary conditions, solve the governing equations of linear elasticity for the displacement field. Then, transform the moving image using the computed displacement field and check the distance measure. Finally, if convergence is not reached, step in the direction minimizing the distance measure by updating the boundary conditions, and repeat the process. A general schematic diagram of the registration process is shown in Figure 2.2.

To solve the governing equations of linear elasticity, the MRST package for MATLAB [29]. MRST, or MATLAB Reservoir Simulation Toolbox, is a SINTEF developed open-source software primarily designed for reservoir modeling and simulations. The module *fvbiot* is used to discretize and solve the equations, with an implementation of the MPSA method explained in subsection 1.4.2. This cell-centered finite volume method is capable of robustly handling spatially varying

and discontinuous Lamé parameters. Implementation details for the fvbiot module can be found in [30]. The optimization is done with the use of MATLABs optimization toolbox, using a quasi-Newton scheme with the BFGS update of the Hessian matrix, as explained in subsection 1.4.1.

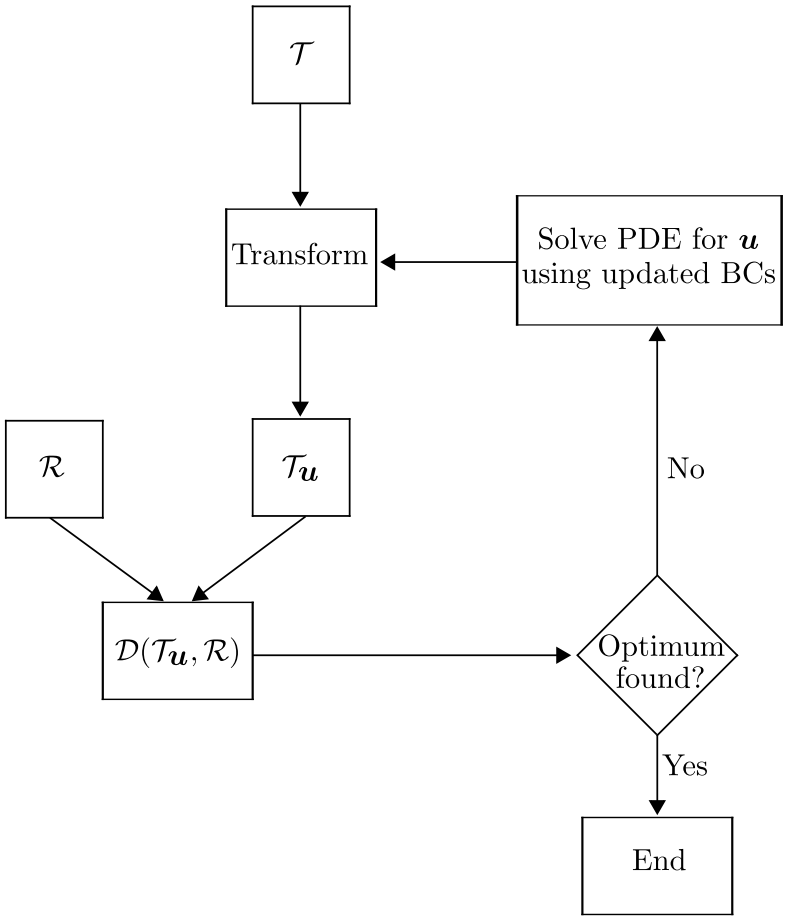

Figure 2.2: Schematic diagram of the BDIR process.

Chapter 3

Experiments

In this chapter, several image registration experiments are done, and is divided as follows. Experiment 1 explores the role of the image force by investigating the agreement between image similarity and displacement field error. In Experiment 2, use of the novel BDIR method is demonstrated on both synthetic and real data. Both time-dependent and independent images are considered. Finally, in Experiment 3, we explore the use of the BDIR method to estimate the Lamé parameters. The results are discussed in section 3.4

Experimental setup

We present the experimental setup and state some information which apply to all experiments.

Image data

The image data[1] is from an unpublished calibration study in collaboration with Department of Radiology Haukeland University Hospital Bergen Norway. The acquisition was performed using T1-weighted 3D spoiled gradient recall echo (GRE) FLASH3D pulse sequence on a 3T Siemens MR scanner. The MRI images were collected under deep breathing to achieve a dynamic sequence containing significant amount of breathing motion. The acquisition parameters were: FOV = 400mm $\times$ 325mm $\times$ 42mm, matrix size = 192 $\times$ 156, pixelsize = 2.08mm $\times$ 2.08mm $\times$ 3.00mm. Total number of time points was 40.

All experiments are done in 2D, meaning we only use the first two spatial dimensions of the image data. Thus we have $\boldsymbol{u} = [u_1(\boldsymbol{x}), u_2(\boldsymbol{x})]$ and $\boldsymbol{x} = [x_1, x_2]$.

[1] Courtesy of Dr. Erik A. Hanson.

Figure 3.1: Moving image $\mathcal{T}(\boldsymbol{x})$ of a human abdomen. The axes are according to a Cartesian coordinate system.

To keep computational time at a reasonable level, the image data was resized by a factor of 0.5. For time-dependent registration, as done in Case 3 of Experiment 2, the moving image is $\mathcal{T}(\boldsymbol{x}, t)$, where all time points of the image data is used. For time-independent registration, the moving image $\mathcal{T}(\boldsymbol{x})$, with domain $\Omega = [0, D_1] \times [0, D_2]$, is taken as a fixed time point of the image data, and is shown in Figure 3.1. As the images are monomodal, we use $\mathcal{D} = \mathcal{D}^{SSD}$ as the distance measure for all experiments.

Forward simulation

We define a *forward simulation* as: Let $\mathcal{I}(\boldsymbol{x})$ be some image. Given some boundary conditions, we solve the elasticity equations from subsection 1.2.5 to obtain the displacement field $\boldsymbol{u}_{forw}$. This is then used to transform the image $\mathcal{I}(\boldsymbol{x})$ into $\mathcal{I}_{forw}(\boldsymbol{x}) = \mathcal{I}(\boldsymbol{x} + \boldsymbol{u}_{forw})$. Experiment 1 uses forward simulations to obtain ground truths, and in Experiment 2 and 3, synthetic cases are considered where the displacement field is obtained from a forward simulation.

Boundary conditions and body forces

Boundary conditions for the elasticity equations are chosen based on assumptions we make about the image data. As the images were collected under deep breathing, we assume the displacement comes solely as a result of respiration. The bottom side is set to zero displacement (homogeneous Dirichlet), the left and right side are set

to zero traction (homogeneous Neumann). The top boundary, which corresponds to the domain

$$\Gamma = \{\boldsymbol{x} \in \Omega : x_2 = D_2\}, \tag{3.1}$$

is prescribed a Dirichlet boundary condition specific to the experiment being done.

For forward simulations, we define the boundary displacement function

$$\boldsymbol{F} : \Gamma \to \mathbb{R}^2, \qquad \boldsymbol{F}(\boldsymbol{x}) = [F_1(\boldsymbol{x}), F_2(\boldsymbol{x})]. \tag{3.2}$$

We assume the displacing force is only asserted vertically. To model this, we set $F_1(\boldsymbol{x}) = 0$ and

$$F_2(\boldsymbol{x}) = M \left(\left(x_1 - \frac{D_1}{2} \right)^2 - \left(\frac{D_1}{2} \right)^2 \right) \left(x_1 - \frac{D_1}{2} \right)^2 \tag{3.3}$$

where M is a scaling factor. $\boldsymbol{F}$ is designed to mimic the displacement introduced as a result of respiration [28]. We have used $M = 10$ in our experiments.

For BDIR, we optimize over the boundary condition on Γ. To do so, we define the boundary displacement function

$$\boldsymbol{g}_D(\boldsymbol{x}; \boldsymbol{p}) = [0, g_D(\boldsymbol{x}; \boldsymbol{p})], \tag{3.4}$$

where

$$g_D : \mathbb{R}^k \to \{f : \Gamma \to \mathbb{R}\}. \tag{3.5}$$

Again, the first component of (3.4) is set to zero as the displacement is assumed to be only asserted vertically. $g_D(\boldsymbol{x}; \boldsymbol{p})$ is set to be a cubic spline interpolating function, which for a parameter $\boldsymbol{p}$, defines a function which can be evaluated at $\boldsymbol{x} \in \Gamma$, giving us the value of $\boldsymbol{u}$ in the vertical direction for every point on the boundary. We have used $k = 20$ in our experiments.

We neglect any body forces, e.g. gravity, and set $\boldsymbol{f}_b = 0$ for all forward simulations and BDIR experiments.

3.1 Experiment 1 - Similarity vs displacement field error

In this experiment, we investigate the role of the image force by exploring the agreement between image similarity and displacement field error when performing traditional elastic registration. As discussed in Chapter 2, the image force act as an unphysical body force driving the registration forward, and we aim to explore the effects it has on the result. In an ideal scenario, we would want the displacement field resulting in the lowest image similarity error to correspond with the lowest displacement field error.

First, we need a known displacement field to compare the registration results against. However, in practice we rarely know the underlying displacement field. We obtain a known displacement field $\boldsymbol{u}_{forw}$ and corresponding transformed image $\mathcal{T}_{forw} = \mathcal{T}(\boldsymbol{x} + \boldsymbol{u}_{forw})$ through a forward simulation.

Next, we want to recover $\mathcal{T}_{forw}$ and $\boldsymbol{u}_{forw}$ through image registration. To do so, we set $\mathcal{T}_{forw}$ as the reference image and $\mathcal{T}$ as the moving image, and register them with traditional elastic registration. By doing so, we obtain $\boldsymbol{u}_{IR}$ and $\mathcal{T}_{IR}(\boldsymbol{x}) = \mathcal{T}(\boldsymbol{x} + \boldsymbol{u}_{IR})$. We are now able to compare the relative displacement field error $E_{disp}(\boldsymbol{u}_{IR}, \boldsymbol{u}_{forw})$ using (1.14) and the relative image intensity error $E_{img}\left(\mathcal{T}_{IR}, \mathcal{T}_{forw}\right)$ using (1.15). The experiment is done with both homogeneous and heterogeneous Lamé parameters in the forward simulation.

3.1.1 Case 1: Homogeneous Lamé parameters

In this case, we perform the forward simulation to get $\boldsymbol{u}_{forw}$ using homogeneous Lamé parameters in the entire domain, specifically $\mu = \lambda = 1$. The moving image $\mathcal{T}$ is shown in Figure 3.1. On the top boundary Γ we, use $\boldsymbol{F}$ from (3.2). Figure 3.2 shows $\mathcal{T}$ with F_2 superimposed. Figure 3.3 visualizes the displacement field $\boldsymbol{u}_{forw}$ along with $\mathcal{T}_{forw}$.

The images are registered with $\mathcal{T}$ and $\mathcal{T}_{forw}$ as moving and reference image respectively, giving us $\boldsymbol{u}_{IR}$ and $\mathcal{T}_{IR}$. This is done with increasing values of μ_{IR} and λ_{IR}, and we calculate E_{disp} and E_{img} for each registration result. Note the difference between $\{\mu, \lambda\}$, which are the first and second Lamé parameter when solving the elasticity equations in the forward simulation, and $\{\mu_{IR}, \lambda_{IR}\}$, which are registration parameters. Table 3.1 lists all relevant registration parameters.

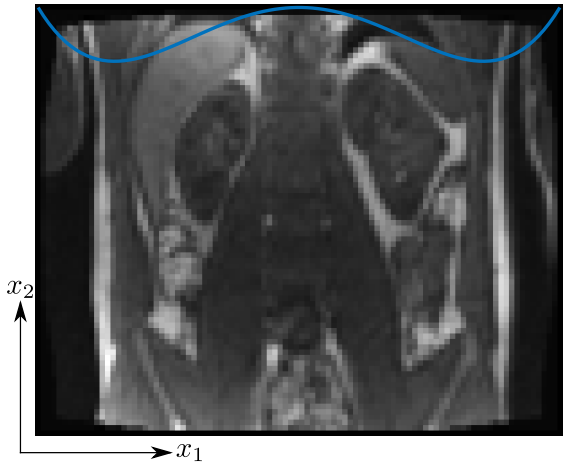

Figure 3.2: Moving image $\mathcal{T}$ with F_2 superimposed on top of the abdomen to simulate breathing motion. The amplitude of F_2 is shown in arbitrary units

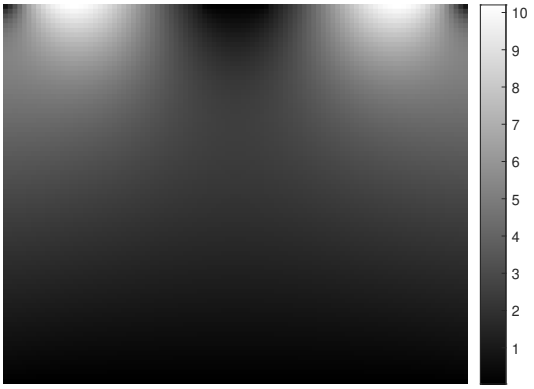

(a) Absolute displacement field $|\boldsymbol{u}_{forw}|$ with homogeneous Lamé parameters. Colorbar in mm.

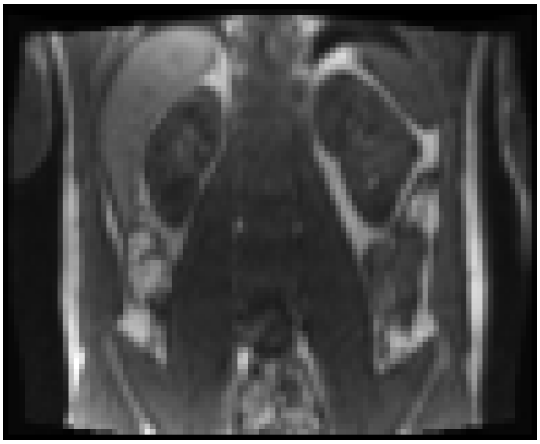

(b) Transformed image $\mathcal{T}_{forw}(\boldsymbol{x}) = \mathcal{T}(\boldsymbol{x} + \boldsymbol{u}_{forw})$.

Figure 3.3: (a) Displacement field and (b) transformed image from forward simulation. Computed with homogeneous Lamé parameters.

Parameter	Symbol	Value
Distance measure	$\mathcal{D}$	SSD
Regularizer	$\mathcal{R}$	Elastic
Regularization parameter	α	1000
1st Lamé parameter	μ_{IR}	$[0.1, 0.2, \ldots, 4]$
2nd Lamé parameter	λ_{IR}	$[0.1, 0.2, \ldots, 4]$

Table 3.1: Registration parameters. μ_{IR} and λ_{IR} are varied from 0.1 to 4 with an increment of 0.1.

Figure 3.4 shows plots of E_{disp} and E_{img} for fixed values μ_{IR} and λ_{IR}. Surface plots are shown in Figure 3.5. We note that E_{disp} has a clear minimum point. However, this does not correspond to a minimum in E_{img}. In fact, E_{img} keeps increasing as we increase μ_{IR} and λ_{IR}. Possible reasons for this behavior will be discussed in section 3.4.

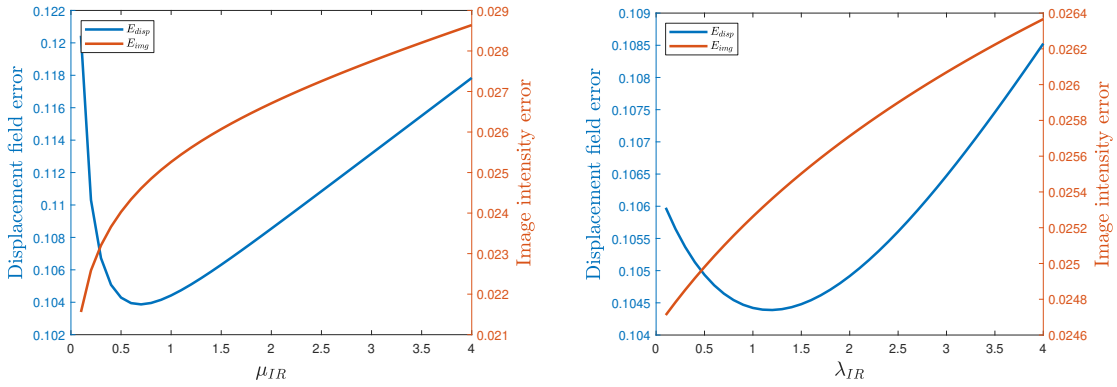

(a) Varying μ_{IR} with fixed $\lambda_{IR} = 1$.

(b) Varying λ_{IR} with fixed $\mu_{IR} = 1$.

Figure 3.4: Values of $E_{disp}\left(\boldsymbol{u}_{IR}, \boldsymbol{u}_{forw}\right)$ in blue and $E_{img}\left(\mathcal{T}_{IR}, \mathcal{T}_{forw}\right)$ in orange for varying values of (a) μ_{IR} and (b) λ_{IR}. The forward simulation is done with homogeneous Lamé parameters.

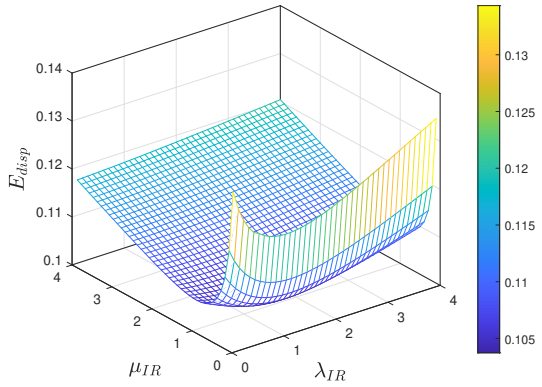

(a) Relative displacement field error $E_{disp}\left(\boldsymbol{u}_{IR}, \boldsymbol{u}_{forw}\right)$ for varying μ_{IR} and λ_{IR}.

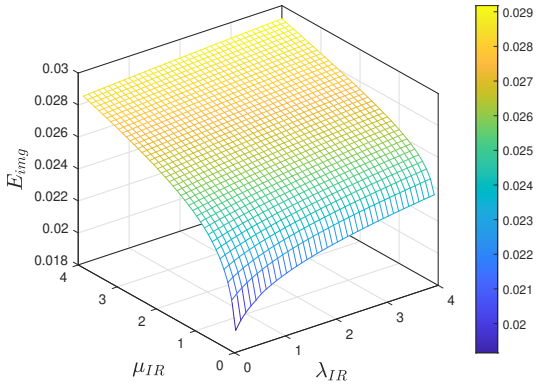

(b) Relative image intensity error $E_{img}\left(\mathcal{T}_{IR}, \mathcal{T}_{forw}\right)$ for varying μ_{IR} and λ_{IR}.

Figure 3.5: Surface plots of E_{disp} and E_{img}. Note the clear minimum of E_{disp} as opposed to E_{img}. Forward simulation is done with homogeneous Lamé parameters.

3.1.2 Case 2: Heterogeneous Lamé parameters

To further investigate the agreement between image similarity and displacement field error, we let $\mu(\boldsymbol{x})$ and $\lambda(\boldsymbol{x})$ vary in space in the forward simulation. This will model a more complex case as we can assign different Lamé parameters to different regions.

Segmentation masks of the spine and both kidneys, shown in Figure 3.6, were manually drawn and assigned values according to Table 3.2. This gives us three distinct regions; spine, kidney, and other organs. "Other organs" consists mostly of the liver and spleen, and reefers to the remaining soft tissue.

It is important to note that the main goal here is to create a more complex displacement field to see how it affects the agreement between image similarity and displacement field error. However, the actual values of $\mu(\boldsymbol{x})$ and $\lambda(\boldsymbol{x})$ are not necessarily physically correct. The values in the region labeled as other organs are arbitrarily set to $\mu = \lambda = 1$, while the kidneys are set to be stiffer than the surrounding tissue. The spine is set to a value of order 10^8 rendering it almost completely rigid. Figure 3.7 visualizes the displacement field $\boldsymbol{u}_{forw}$. We see that the region corresponding to the spine has zero displacement, and the kidneys displace differently than the surrounding organs due to its higher Lamé parameters.

The registration is done with the same parameters as in Case 1, with registration parameters listed in Table 3.1. From the results in Figure 3.8, we again note that the minimum of E_{disp} does not correspond to a minimum of E_{img}. This is further discussed in section 3.4.

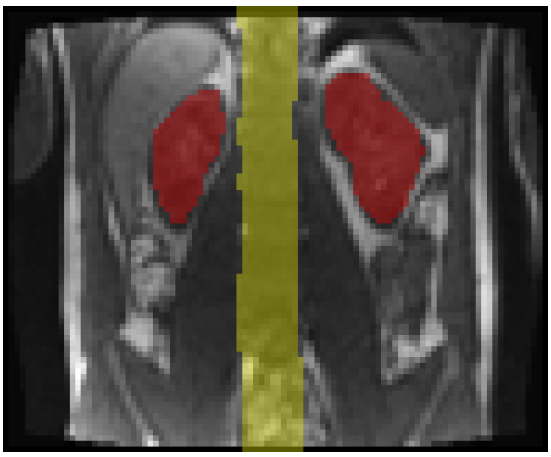

Figure 3.6: Manual segmentation of the MRI image. Spine in yellow and kidneys in red. Tissue specific Lamé parameters were assigned according to the segmentation

Parameter	Kidney	Spine	Other organs
μ	4	1×10^8	1
λ	2	1×10^8	1

Table 3.2: Lamé parameters for kidney, spine and generic organ.

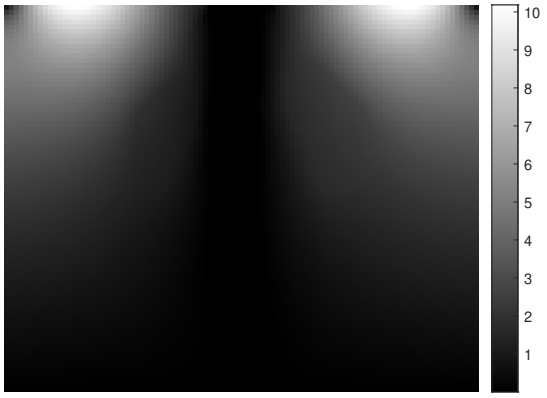

Figure 3.7: Absolute displacement field $|\boldsymbol{u}_{forw}|$ with heterogeneous Lamé parameters. Notice there is no deformation along the spine, and the outline of the stiffer kidneys are visible. Colorbar in mm.

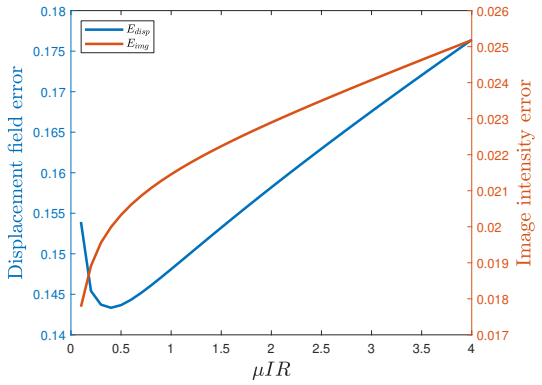

(a) Varying μ_{IR} with fixed $\lambda_{IR} = 1$

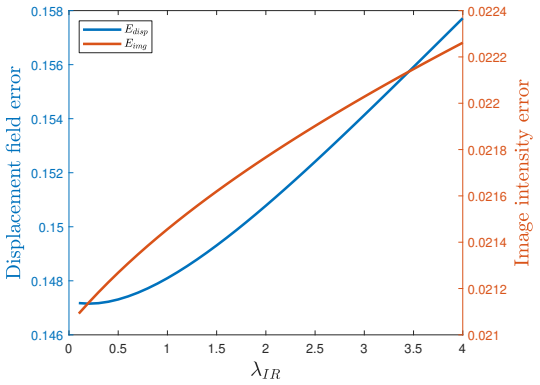

(b) Varying λ_{IR} with fixed $\mu_{IR} = 1$

Figure 3.8: Values of $E_{disp}\left(\boldsymbol{u}_{IR}, \boldsymbol{u}_{forw}\right)$ in blue and $E_{img}\left(\mathcal{T}_{IR}, \mathcal{T}_{forw}\right)$ in orange for varying values of (a) μ_{IR} and (b) λ_{IR}. The forward simulation is done with heterogeneous Lamé parameters.

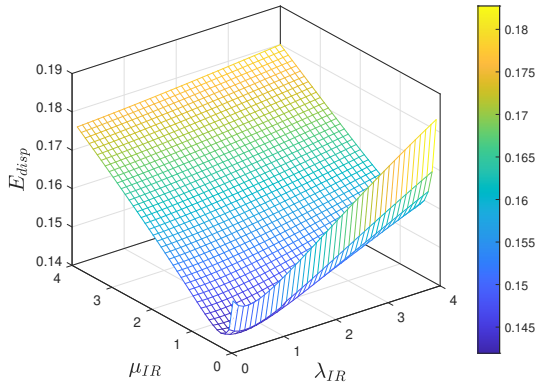

(a) Relative displacement field error $E_{disp}\left(\boldsymbol{u}_{IR}, \boldsymbol{u}_{forw}\right)$ for varying μ_{IR} and λ_{IR}.

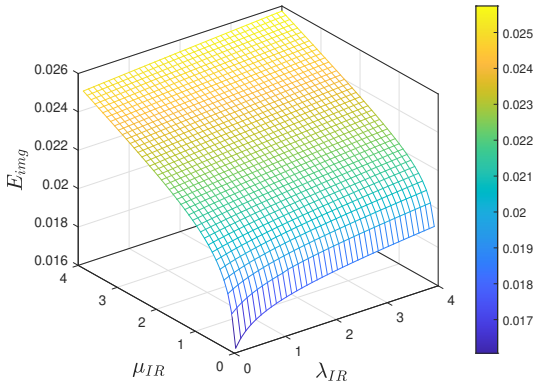

(b) Relative image intensity error $E_{img}\left(\mathcal{T}_{IR}, \mathcal{T}_{forw}\right)$ for varying μ_{IR} and λ_{IR}.

Figure 3.9: Surface plots of E_{disp} and E_{img}. Forward simulation is done with heterogeneous Lamé parameters.

3.2 Experiment 2 - Boundary-driven image registration

In this experiment, we demonstrate the capabilities of the novel BDIR method, presented in section 2.2. Both synthetic and real cases are considered, where in the latter case, both time-dependent and independent images are registered. The results are compared to the ones produced by traditional elastic image registration. The minimization problem defining the elastic BDIR method is repeated here for ease of reading:

$$\begin{aligned} \min_{\boldsymbol{p}} \quad & \mathcal{D}(\mathcal{T}_{\boldsymbol{u}}, \mathcal{R}) \\ \text{s.t.} \quad & \boldsymbol{f}_b(\boldsymbol{x}) + \nabla \cdot \left(2\mu\boldsymbol{\varepsilon}(\boldsymbol{u}) + \lambda(\nabla \cdot \boldsymbol{u})\boldsymbol{I}\right) = 0 \quad \text{in} \quad \Omega, \\ & \qquad\qquad \boldsymbol{u} = \boldsymbol{g}_D(\boldsymbol{x}; \boldsymbol{p}) \quad \text{on} \quad \partial\Omega_D, \\ & \qquad\qquad \boldsymbol{\sigma} \cdot \boldsymbol{n} = \boldsymbol{g}_N(\boldsymbol{x}; \boldsymbol{p}) \quad \text{on} \quad \partial\Omega_N, \end{aligned} \tag{3.6}$$

where $\mathcal{T}_{\boldsymbol{u}}$ and $\mathcal{R}$ are transformed moving image and reference image respectively, $\boldsymbol{f}_b(\boldsymbol{x})$ are body forces, $\boldsymbol{g}_D(\boldsymbol{x}; \boldsymbol{p})$ and $\boldsymbol{g}_N(\boldsymbol{x}; \boldsymbol{p})$ are boundary conditions. Note the dependency of the optimizing variable $\boldsymbol{p}$. Domains $\partial\Omega_D$ and $\partial\Omega_N$ are parts of the boundary prescribed with Dirichlet and Neumann boundary conditions respectively, and the full boundary of the domain Ω is $\partial\Omega = \partial\Omega_D \cup \partial\Omega_N$.

3.2.1 Case 1: Synthetic displacement

To demonstrate the validity of the registration method, we construct a case where the displacement is known, and try to recover it with BDIR. The purpose of this test is to ensure that the method gives reasonable results in predictable cases.

The known displacement field is obtained by a forward simulation, giving us $\boldsymbol{u}_{forw}$ and $\mathcal{T}_{forw} = \mathcal{T}(\boldsymbol{x} + \boldsymbol{u}_{forw})$. This is done with $\boldsymbol{F}$ from (3.2) as the top Dirichlet boundary condition for domain Γ in (3.1). Further, we use homogeneous Lamé parameter equal to 1 for the entire domain.

$\mathcal{T}_{forw}$ and $\boldsymbol{u}_{forw}$ are reconstructed using BDIR, setting $\mathcal{T}_{forw}$ as the reference image, and $\mathcal{T}$ as the moving image. For the domain Γ from (3.1), corresponding to the top boundary, we use $\boldsymbol{g}_D$ from (3.4). As we have homogeneous Neumann conditions on $\partial\Omega_N$, we set $\boldsymbol{g}_N = 0$. Finally, the Lamé parameters are set to be homogeneous equal to 1. The BDIR results gives us $\boldsymbol{u}_{BDIR}$ and $\mathcal{T}_{BDIR} = \mathcal{T}(\boldsymbol{x} + \boldsymbol{u}_{BDIR})$.

Figure 3.10 shows the resulting boundary displacement, g_D, found to satisfy (3.6), along with F_2. Notice that they are nearly identical. The relative error between boundaries were found to be $\frac{\|\boldsymbol{F} - \boldsymbol{g}_D\|_2}{\|\boldsymbol{F}\|_2} = 3.89 \times 10^{-3}\,\%$. Further, the relative displacement field error $E_{disp}(\boldsymbol{u}_{BDIR}, \boldsymbol{u}_{forw}) = 6.50 \times 10^{-2}\,\%$ and relative image in-

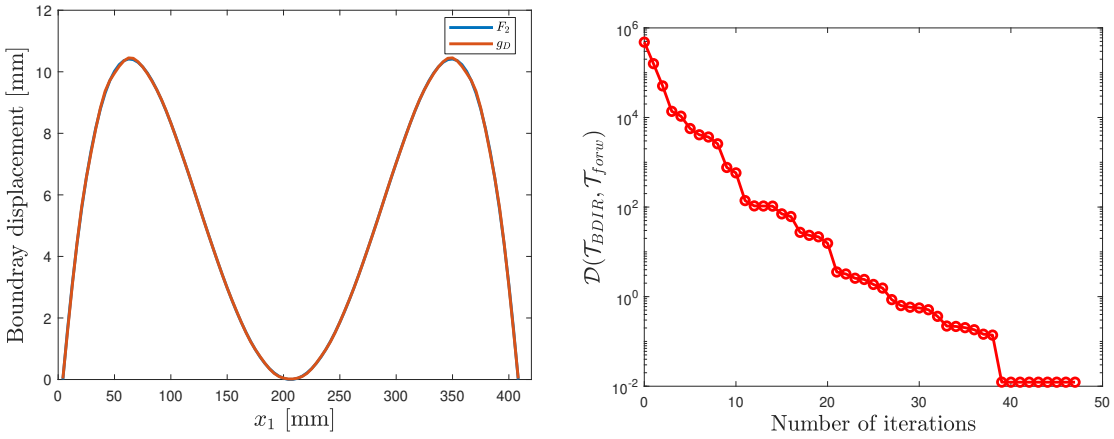

(a) (b)

Figure 3.10: (a): Boundary displacement used in the forward simulation F_2 and boundary g_D found to satisfy (3.6). Note that they lie on-top of each other. (b): Convergence plot

tensity error $E_{img}(\mathcal{T}_{BDIR}, \mathcal{T}_{forw}) = 2.38 \times 10^{-3}\,\%$, which both suggest a successful registration.

3.2.2 Case 2: Real displacement - Time-independent registration

A real case using the MRI image data is now considered. A time-independent image is registered to a reference image using BDIR. As the images are taken from an MRI-scan of the human abdomen, the true displacement is now unknown.

The reference and moving images, $\mathcal{R}$ and $\mathcal{T}$, can be seen in Figure 3.11. They differ from each other as a result of the person breathing during the imaging process. The displacement is assumed to be caused solely by the respiration force, which we again model by using $\boldsymbol{g}_D$ from equation (3.4) as the top boundary condition. Homogeneous Lamé parameters equal to 1 is used.

Figure 3.12a shows the resulting boundary displacement. Note that g_D is close to zero where the spine lies, and has maxima located between the spine and left and right boundary. Figure 3.12b visualizes the resulting displacement field.

In Figure 3.13, two different visualizations of the BDIR results are shown. The colored visualization shows a magenta/green color where the images differ in intensity, while the difference visualization shows $|\mathcal{T}_{BDIR} - \mathcal{R}|$. The results are compared to the ones produced by a traditional elastic registration approach. In terms of relative intensity error E_{img}, the BDIR method achieved an error of 19.2%

(25.1% decrease), while the traditional method achieved an error of 11.5% (53.8% decrease). The results will be discussed in section 3.4.

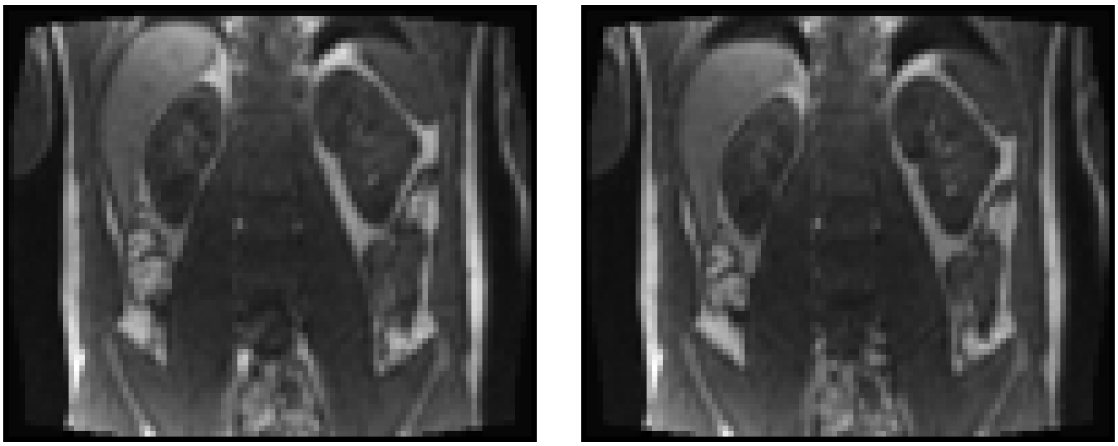

(a) $\mathcal{T}$ (b) $\mathcal{R}$

Figure 3.11: (a) Moving image and (b) reference image used for single image BDIR. They differ from each other as a result of the person breathing during the imaging process.

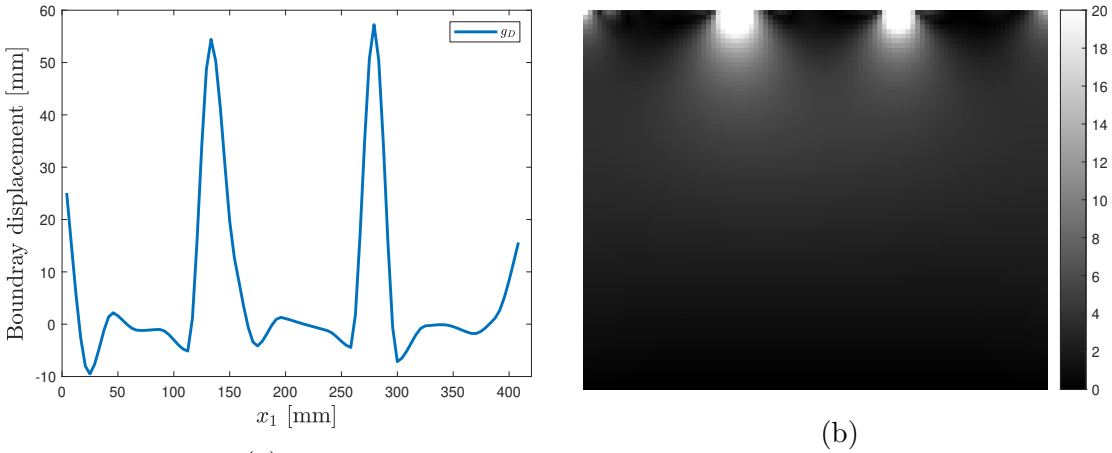

(a) (b)

Figure 3.12: Registration result: (a) Optimal boundary displacement found to satisfy the BDIR problem (3.6), and (b) the corresponding absolute displacement field. Colorbar in mm.

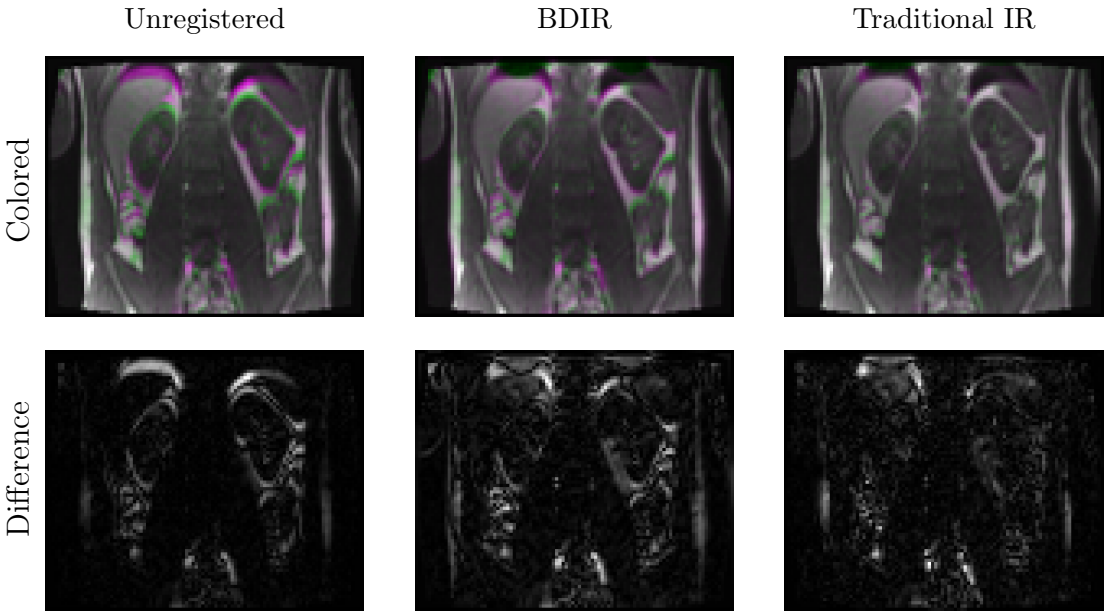

Figure 3.13: Visualizations of the BDIR results. First column shows the unregistered images, the second is registered with BDIR, and the last is registered with traditional elastic registration.

3.2.3 Case 3: Real displacement - Time-dependent registration

The time-dependent image $\mathcal{T}(\boldsymbol{x}, t)$ from the MRI data is now registered using BDIR. Registering time-dependent images is one of the most common tasks in medical image registration, and is a suitable way of demonstrating the capabilities of the method.

The MRI image is registered in sequence, meaning all time-points are registered with Figure 3.11b as the reference $\mathcal{R}(\boldsymbol{x}) = \mathcal{T}(\boldsymbol{x}, t = 0)$. Registration of $\mathcal{T}(\boldsymbol{x}, t)$ gives us the registered image $\mathcal{T}_{BDIR}(\boldsymbol{x}, t)$. To illustrate the results, vertical slices at different spacial positions are taken from $\mathcal{T}$ and $\mathcal{T}_{BDIR}$ from each time-point. The slices are displayed along the horizontal axis, which can be seen as a time-axis. Figure 3.14 shows the results. Notice how in the unregistered image, wave-like patterns can be seen. This is a result of the breathing cycle of the person being scanned. Straight horizontal lines in the registration result indicate spacial alignment. To compare the results, the same image was registered using the traditional method. In terms of average relative image intensity error, BDIR achieved an error of 15.6%, while the traditional method achieved an error of 10.2%.

Figure 3.15 shows the found optimal boundary displacement g_D for several different

time instances. Here we can clearly see the periodic nature of the breathing cycle.

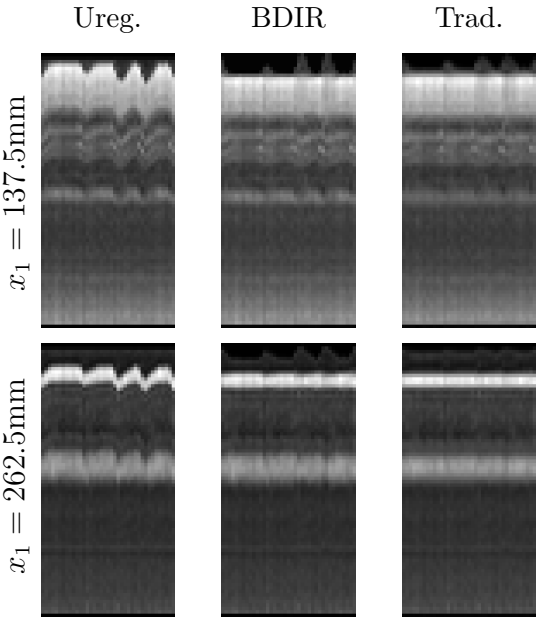

Figure 3.14: Vertical cuts through the images at two different spacial positions. First column shows slices form the unregistered image, the second is from the registered image using BDIR, and the last is registered using the traditional elastic method.

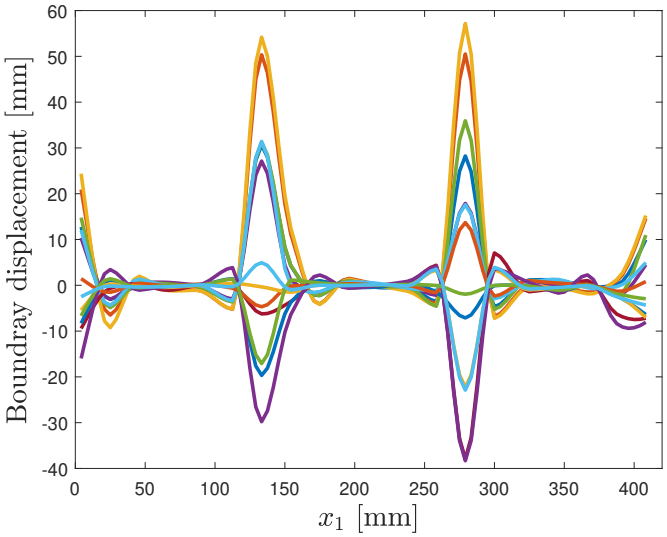

Figure 3.15: Optimal boundary displacement shown in different colors for various time instances. .

3.3 Experiment 3 - Tissue parameter estimation

In this experiment, we expand on the BDIR minimization problem, and simultaneously search for optimal boundary conditions and optimal tissue parameters, i.e. the Lamé parameters $\mu(\boldsymbol{x})$ and $\lambda(\boldsymbol{x})$. This greatly increases the complexity of the problem, as the Lamé parameters can significantly impact the boundary condition values. Being able to estimate tissue parameters with non-invasive tools can potentially improve the diagnosis of diseases like chronic kidney disease, see e.g. articles by Hodneland et al. [28, 5]. With this experimental setup, we do not intend to accurately estimate physically correct tissue parameter values, but rather explore the effects of using image registration to optimize over the parameters.

A synthetic case is first considered, where a known displacement field, with known Lamé parameters, is used to transform an image. The displacement field, and specifically the Lamé parameters, are attempted reconstructed. A real case, with unknown displacement, is then considered, where different setups are tested to explore the effects of the addition to the problem.

With the addition of the Lamé parameters, the BDIR method reads

$$\begin{aligned} \min_{\boldsymbol{p},\,\mu,\,\lambda} \quad & \mathcal{D}(\mathcal{T}_{\boldsymbol{u}}, \mathcal{R}) \\ \text{s.t.} \quad & \boldsymbol{f}_b(\boldsymbol{x}) + \nabla \cdot \big(2\mu(\boldsymbol{x})\boldsymbol{\varepsilon}(\boldsymbol{u}) + \lambda(\boldsymbol{x})(\nabla \cdot \boldsymbol{u})\boldsymbol{I}\big) = 0 \quad \text{in} \quad \Omega, \\ & \qquad\qquad \boldsymbol{u} = \boldsymbol{g}_D(\boldsymbol{p}) \quad \text{on} \quad \partial\Omega_D, \\ & \qquad\qquad \boldsymbol{\sigma} \cdot \boldsymbol{n} = \boldsymbol{g}_N(\boldsymbol{p}) \quad \text{on} \quad \partial\Omega_N. \end{aligned} \tag{3.7}$$

To reduce computational complexity, we add further constraints to the problem by modeling the Lamé parameters as piecewise constant, and only optimize over the value inside a region of interest.

3.3.1 Case 1: Synthetic displacement

For the moving image $\mathcal{T}(\boldsymbol{x})$, we define a subdomain Ω_{kid} according to the segmentation shown in Figure 3.16. For the forward simulation, the Lamé parameters are set to

$$\mu_{forw}(\boldsymbol{x}) = \begin{cases} 4, & \text{if } \boldsymbol{x} \in \Omega_{kid} \\ 1, & \text{otherwise,} \end{cases} \qquad \text{and} \qquad \lambda_{forw}(\boldsymbol{x}) = \begin{cases} 2, & \text{if } \boldsymbol{x} \in \Omega_{kid} \\ 1, & \text{otherwise.} \end{cases}$$

The boundary displacement function $\boldsymbol{F}$ from (3.2) is set as the top Dirichlet boundary condition. The forward simulation gives us $\boldsymbol{u}_{forw}$ and $\mathcal{T}_{forw}$

Solving (3.7), we obtain $\boldsymbol{u}_{BDIR}$ and $\mathcal{T}_{BDIR}$. Optimal Lamé parameters found were $\mu = 4.000597$ and $\lambda = 1.99615$ which is corresponds well with μ_{forw} and λ_{forw}.

Figure 3.16: Manual segmentation of the kidneys, corresponding to Ω_{kid}, shown in red.

Further, the relative boundary error was found to be $\frac{\|\boldsymbol{F}-\boldsymbol{g}_D\|_2}{\|\boldsymbol{F}\|_2} = 3.89 \times 10^{-3}\,\%$. Relative displacement field error $E_{disp}(\boldsymbol{u}_{BDIR}, \boldsymbol{u}_{forw}) = 6.49 \times 10^{-2}\,\%$ and relative image intensity error $E_{img}(\mathcal{T}_{BDIR}, \mathcal{T}_{forw}) = 2.39 \times 10^{-3}\,\%$ both indicate a successful registration.

3.3.2 Case 2: Real displacement

The MRI image data is registered with BDIR meaning the true displacement field and Lamé parameters are unknown. This experiment is similar to Case 2 in Experiment 2, with the addition of optimization over the Lamé parameters.

As suggested by S. Kabus [31], the Lamé parameters should be set in a relative way, as the reported values for the same tissue-type varies a lot across different literature. In our experimental setup, the values of $\mu(\boldsymbol{x}), \lambda(\boldsymbol{x}) \, \forall \, \boldsymbol{x} \notin \Omega_{kid}$ are arbitrarily set to 1, and we therefore have

$$\mu(\boldsymbol{x}) = \begin{cases} \mu_{kid}, & \text{if } \boldsymbol{x} \in \Omega_{kid} \\ 1, & \text{otherwise,} \end{cases} \qquad \text{and} \qquad \lambda(\boldsymbol{x}) = \begin{cases} \lambda_{kid}, & \text{if } \boldsymbol{x} \in \Omega_{kid} \\ 1, & \text{otherwise,} \end{cases}$$

where μ_{kid} and λ_{kid} are optimized over. This means that the meaning these parameters should be seen as a stiffness value relative to the surround tissue, rather than a physically correct value.

The moving and reference image from Figure 3.11, with the kidney segmentation from Figure 3.16, are registered with BDIR by solving solving (3.7). We define four different cases to explore the interplay between the parameters:

A Reference case with homogeneous parameters, i.e $\mu_{kid} = \lambda_{kid} = 1$.

B Both μ_{kid} and λ_{kid} is optimized over.

C λ_{kid} is held constant equal to 1. μ_{kid} is optimized over.

D μ_{kid} is held constant equal to 1. λ_{kid} is optimized over.

For each case we note the relative intensity error E_{img}, the bulk modulus $K_{kid} = \lambda_{kid} + \frac{2\mu_{kid}}{3}$, and the average volume changes of the kidneys, i.e. the mean of $\nabla \cdot \boldsymbol{u}$ for $\boldsymbol{x} \in \Omega_{kid}$. Table 3.3 lists the results, which will be discussed in next section.

Case	SSD$\times 10^6$	$E_{img} \times 100\%$	μ_{kid}	λ_{kid}	K_{kid}	$\overline{\nabla \cdot \boldsymbol{u}}$
Ureg.	1.297	-	-	-	-	-
A	0.728	19.18%	1	1	1.67	2.01×10^{-4}
B	0.718	19.06%	3.37	4.97×10^{-4}	2.25	1.81×10^{-4}
C	0.720	19.07%	4.54	1	4.02	1.31×10^{-4}
D	0.724	19.13%	1	3.82×10^{-7}	6.67×10^{-1}	2.97×10^{-4}

Table 3.3: Registration results for the four different cases. $\overline{\nabla \cdot \boldsymbol{u}}$ denotes the average divergence of $\boldsymbol{u}$ in Ω_{kid}.

3.4 Discussion

The results from each experiment are discussed and in this section.

Experiment 1

In Experiment 1, we highlighted the lack of agreement between image similarity and displacement field error using traditional registration methods.. From Figure 3.4 and Figure 3.9, it is clear that when varying μ_{IR} and λ_{IR}, the solution giving minimum displacement field error does not correspond with the minimum image similarity error. In fact, E_{img} keeps decreasing as we decrease μ_{IR} and λ_{IR}, and one possible reason for this is clear. Looking at the joint energy functional to be minimized in equation (2.4), we see that lowering the regularization parameters puts more emphasis on the similarity term, and as a consequence, less on the smoothness of the displacement field. Hence we see a decrease in image similarity error. Lowering the parameters even further would eventually defeat the purpose of regularization, and we could expect a decrease of E_{img} along with a highly unphysical displacement field, until the solver is unable to escape a local minimum.

In Case 2 of Experiment 1, the same setup is repeated, but with a more complex displacement field as the ground truth. A similar behavior as the first case is found, as shown in Figure 3.8 and Figure 3.9. We note that values of E_{disp} is higher for all values compared to Case 1. Furthermore, we note that lower values of μ_{IR} and λ_{IR} is needed to minimize E_{disp}. A possible reason for this is the fact that the Lamé parameters are constant for the entire domain in traditional elastic registration, and needs to be set to a lower value to compensate for the larger local changes in $\nabla \boldsymbol{u}$ in Case 2 compared to Case 1.

The results found in this experiment illustrate that unphysical image-derived forces will align images with a relative similarity error of approximately only 2%, while at the same time having a relative displacement field error of approximately 10%. Note that the results are sensitive to the specific images used, specifically the amount of details in the image. Similar studies have found that traditional registration methods align images to the same degree as ours, but with a relative displacement field error as high as 40% [5, 28, 32].

Experiment 2

In Experiment 2, the capabilities of the novel BDIR scheme is demonstrated. A synthetically deformed image where the boundary conditions and displacement field were known, was registered using the scheme. From the results in Figure 3.10, we see that the boundary displacement found is close to the true displacement, with

a relative error of order $10^{-3}\%$, and relative displacement field error E_{disp} of order $10^{-2}\%$. It is important to note that this test can be seen as a so-called inverse crime verification test, as we are optimizing with the same numerical implementation as the ground truth was calculated with. Is is done to ensure that the method gives reasonable results in predictable cases. Relative displacement field error found with BDIR is significantly better than the traditional methods, however, the results are not directly comparable because of the inverse-crime bias.

Using a real dataset, MRI images of the human abdomen are registered with the BDIR method. Both time-independent and dependent images are registered. From Figure 3.13 and Figure 3.14 we see that the registration produces satisfying visual results. In particular, the latter figure illustrates that BDIR produces comparable visual results to traditional elastic registration.

In terms of reduction of the SSD, i.e. relative intensity error, traditional elastic registration produces superior results. This is not surprising, considering that the traditional approach has significantly higher degrees of freedom in the optimization, where every point in the moving image can individually be displaced. This is a direct result of the unphysical image force.

From Figure 3.15 we see that the found optimal boundary displacement is consistently close to zero where the spine lies, and has maxima located between the spine and left and right boundary. As we know the displacement is caused by deep breathing, these results are in line with what we would expect.

The motivation for the BDIR method was to avoid the use of unphysical image forces, and put more emphasis on the physical correctness of the resulting displacement field, which was achieved by placing the source of displacement on the boundaries of the domain. Unfortunately, as pointed out in subsection 1.1.5, evaluation of the displacement field is difficult as the real displacement field is in practice never known.

Experiment 3

In Experiment 3, we expand on the BDIR method to include optimization over the Lamé parameters in selected regions on interest. A synthetic inverse-crime test was performed, similar to the one in Experiment 2. The Lamé parameters of the kidneys were recovered with an error of order 10^{-3}.

Several cases were considered when optimizing over the Lamé parameters of the kidneys to explore the interplay. From the results in Table 3.3, we note that the lowest relative intensity error was achieved when optimizing over both parameters, however, the difference between cases were found to be small. The average volume

changes saw little variation in the different cases, which is desirable for the robustness of the method, and values found are comparable to the ones in [28]. Finally, we note that the highest bulk modulus found, corresponds to the lowest average volume changes, and vice versa, which is consistent with what we could expect.

Chapter 4

Conclusions and Outlook

This thesis has two contributions. The effects of unphysical image-derived forces are explored and highlighted, and a novel image registration method is presented.

In light of the image force, we investigated the usage of traditional elastic registration to accurately estimate displacement fields. Results from Experiment 1 in section 3.1 show that the agreement between relative image similarity error and relative displacement field error is poor, and the registration parameters strongly influence the result. This is unavoidable, as the method tries to balance an unphysical image force which tries to minimize similarity error, and a physical measure of the displacement field.

A novel image registration approach was presented, the boundary-driven image registration method, motivated by the need for a method where the resulting displacement comes as a result of a force/displacement on the boundary, and avoiding the image force. To validate the method, several experiments were done on both synthetic and real data. The results from Experiment 2 in section 3.2 indicate satisfactory visual results, comparable to traditional elastic registration, and performs well in synthetic cases. The resulting displacement fields are guaranteed to be physically plausible and obeys the governing equations of linear elasticity. However, this is at the cost of a worse performance in terms of image similarity error.

The BDIR method was expanded to explore the effects of optimizing over the Lamé parameters and boundary conditions simultaneously. The results from section 3.3 indicate that we achieve a better registration in terms of image similarity error, and we obtain relative tissue parameter values. This experiment serves mainly as a proof of concept, and should be further investigated by adding more regions of interest.

The proposed method has the potential to be further developed into a more robust registration algorithm to accurately estimate the physical displacement that has occurred and the material parameters. Nevertheless, it has several limitations which needs to be considered. The biggest limitation is computational cost. As we assume the displacement is only driven by a force/displacement on the boundary, the tissue parameters should be spatially varying to a much higher degree that what is done in this thesis, in order to obtain a more physically correct displacement field. However, optimizing over $\mu(\boldsymbol{x}), \lambda(\boldsymbol{x}) \ \forall \ \boldsymbol{x} \in \Omega$ would require too much possessing power with the current implementation. The MRST package was preferred in this thesis as it allowed for rapid prototyping and robust solvers, but it was not used to its full potential. The possibility of implementing automatic differentiation [33, 34], possibly with MRSTs own automatic differentiation framework [29], should be explored in order to allow for higher degrees of freedom in the minimization problem, while at the same time keeping the computational cost at a reasonable level.

Finally, we risk loosing a significant amount of information when only performing the registration in 2D. Hence, an extension to 3D registration [8, 35] should be investigated. This could especially impact the results from the tissue parameter estimation experiment, as tissue can expand/contract in every direction.

Bibliography

[1] B. Zitová and J. Flusser, "Image registration methods: a survey," *Image and Vision Computing*, vol. 21, pp. 977–1000, oct 2003.

[2] A. A. Goshtasby, *Theory and Applications of Image Registration*. WILEY, Aug. 2017.

[3] J. Modersitzki, *Fair: Flexible Algorithms for Image Registration*. CAMBRIDGE, Nov. 2009.

[4] F. Sauer, "Image registration: Enabling technology for image guided surgery and therapy," in *2005 IEEE Engineering in Medicine and Biology 27th Annual Conference*, IEEE, 2005.

[5] E. Hodneland, E. Hanson, A. Z. Munthe-Kaas, A. Lundervold, and J. M. Nordbotten, "Physical models for simulation and reconstruction of human tissue deformation fields in dynamic MRI," *IEEE Transactions on Biomedical Engineering*, vol. 63, pp. 2200–2210, oct 2016.

[6] J. Modersitzki, *Numerical Methods for Image Registration*. Oxford University Press, dec 2003.

[7] E. Haber and J. Modersitzki, "Intensity gradient based registration and fusion of multi-modal images," in *Medical Image Computing and Computer-Assisted Intervention – MICCAI 2006*, pp. 726–733, Springer Berlin Heidelberg, 2006.

[8] E. Hodneland, A. Lundervold, J. Rørvik, and A. Z. Munthe-Kaas, "Normalized gradient fields for nonlinear motion correction of DCE-MRI time series," *Computerized Medical Imaging and Graphics*, vol. 38, pp. 202–210, apr 2014.

[9] G. E. Ladas, *Differential equations in abstract spaces*. New York: Academic Press, 1972.

[10] C. Broit, *Optimal Registration of Deformed Images*. PhD thesis, University of Pensylvania, 1981.

[11] G. E. Christensen, *Deformable shape models for anatomy*. PhD thesis, Washington University, 1994.

[12] B. Fischer and J. Modersitzki, "A unified approach to fast image registration and a new curvature based registration technique," *Linear Algebra and its Applications*, vol. 380, pp. 107–124, mar 2004.

[13] B. Fischer and J. Modersitzki, "Fast inversion of matrices arising in image processing," *Numerical Algorithms*, vol. 22, no. 1, pp. 1–11, 1999.

[14] B. Fischer and J. Modersitzki, "Curvature based image registration," *Journal of Mathematical Imaging and Vision*, 2003.

[15] T. Rohlfing, "Image similarity and tissue overlaps as surrogates for image registration accuracy: Widely used but unreliable," *IEEE Transactions on Medical Imaging*, vol. 31, pp. 153–163, feb 2012.

[16] S. Timoshenko, *Theory of elasticity*. New Delhi, India: McGraw-Hill Education, 2010.

[17] J. Lubliner, *Introduction to solid mechanics : an integrated approach*. New York, NY: Springer, 2014.

[18] S. Tarafdar, A. Nakahara, T. Dutta, S. Kitsunezaki, and L. Goehring, *Desiccation Cracks and their Patterns*. Wiley VCH Verlag GmbH, Apr. 2015.

[19] E. B. Tadmor, R. E. Miller, and R. S. Elliott, *Continuum Mechanics and Thermodynamics*. Cambridge University Press, Aug. 2017.

[20] J. N. Reddy, *An Introduction to Continuum Mechanics*. Cambridge University Press, Oct. 2007.

[21] E. W. Chaves, *Notes on Continuum Mechanics*. Springer Netherlands, Mar. 2013.

[22] C. D. Coman, *Continuum Mechanics and Linear Elasticity*. Springer Netherlands, Nov. 2019.

[23] S. W. Jorge Nocedal, *Numerical Optimization*. Springer-Verlag GmbH, Sept. 2006.

[24] B. G. T. Eligius M. T. Hendrix, *Introduction to Nonlinear and Global Optimization*. Springer New York, Apr. 2010.

[25] I. Aavatsmark, "An introduction to multipoint flux approximations for quadrilateral grids," *Computational Geosciences*, vol. 6, no. 3/4, pp. 405–432, 2002.

[26] J. M. Nordbotten, "Cell-centered finite volume discretizations for deformable porous media," *International Journal for Numerical Methods in Engineering*, vol. 100, pp. 399–418, aug 2014.

[27] R. Fletcher, *Practical methods of optimization*. Chichester New York: Wiley, 1987.

[28] E. Hodneland, E. Keilegavlen, E. A. Hanson, E. Andersen, J. A. Monssen, J. Rorvik, S. Leh, H.-P. Marti, A. Lundervold, E. Svarstad, and J. M. Nordbotten, "In vivo detection of chronic kidney disease using tissue deformation fields from dynamic MR imaging," *IEEE Transactions on Biomedical Engineering*, vol. 66, pp. 1779–1790, jun 2019.

[29] K.-A. Lie, *An Introduction to Reservoir Simulation Using MATLAB/GNU Octave*. Cambridge University Press, June 2019.

[30] J. Varela, "Implementation of an mpfa/mpsa-fv solver for the unsaturated flow in deformable porous media," Master's thesis, University of Bergen, 2018.

[31] A. Franz, B. Fischer, and S. Kabus, "Spatially varying elasticity in image registration," *Methods of Information in Medicine*, vol. 46, no. 03, pp. 287–291, 2007.

[32] H.-P. Lee, M. C. Lin, and M. Foskey, "Physically-based validation of deformable medical image registration," in *Medical Image Computing and Computer-Assisted Intervention – MICCAI 2008*, pp. 830–838, Springer Berlin Heidelberg, 2008.

[33] A. Griewank, "On automatic differentiation," 02 1997.

[34] M. Bartholomew-Biggs, S. Brown, B. Christianson, and L. Dixon, "Automatic differentiation of algorithms," *Journal of Computational and Applied Mathematics*, vol. 124, pp. 171–190, dec 2000.

[35] A. D. Merrem, F. G. Zöllner, M. Reich, A. Lundervold, J. Rorvik, and L. R. Schad, "A variational approach to image registration in dynamic contrast-enhanced MRI of the human kidney," *Magnetic Resonance Imaging*, vol. 31, pp. 771–777, jun 2013.